SANDIA REPORT

SAND 2013-2526
Unlimited Release
March 2013

Materials Corrosion of High Temperature Alloys Immersed in 600°C Binary Nitrate Salt

Alan M. Kruizenga, David D. Gill, Marianne LaFord

Prepared by
Sandia National Laboratories
Albuquerque, New Mexico 87185 and Livermore, California 94550

Sandia National Laboratories is a multi-program laboratory managed and operated by Sandia Corporation, a wholly owned subsidiary of Lockheed Martin Corporation, for the U.S. Department of Energy's National Nuclear Security Administration under contract DE-AC04-94AL85000.

Issued by Sandia National Laboratories, operated for the United States Department of Energy by Sandia Corporation.

Available to DOE and DOE contractors from
U.S. Department of Energy
Office of Scientific and Technical Information
P.O. Box 62
Oak Ridge, TN 37831

Telephone: (865) 576-8401
Facsimile: (865) 576-5728
E-Mail: reports@adonis.osti.gov
Online ordering: http://www.osti.gov/bridge

Available to the public from
U.S. Department of Commerce
National Technical Information Service
5285 Port Royal Rd.
Springfield, VA 22161

Telephone: (800) 553-6847
Facsimile: (703) 605-6900
E-Mail: orders@ntis.fedworld.gov
Online order: http://www.ntis.gov/help/ordermethods.asp?loc=7-4-0#online

SAND2013-2526
Unlimited Release
March 2013

Materials Corrosion of High Temperature Alloys Immersed in 600°C Binary Nitrate Salt

Alan M. Kruizenga[1], David D. Gill[2], Marianne LaFord[1]
1. 8223: Materials Chemistry
2. 6123: Concentrating Solar Technologies
Sandia National Laboratories
P.O. Box 0969
Livermore, California 94551-MS9403

Abstract

Thirteen high temperature alloys were immersion tested in a 60/40 binary nitrate salt. Samples were interval tested up to 3000 hours at 600°C with air as the ullage gas. Chemical analysis of the molten salt indicated lower nitrite concentrations present in the salt, as predicted by the equilibrium equation. Corrosion rates were generally low for all alloys. Corrosion products were identified using x-ray diffraction and electron microprobe analysis. Fe-Cr based alloys tended to form mixtures of sodium and iron oxides, while Fe-Ni/Cr alloys had similar corrosion products plus oxides of nickel and chromium. Nickel based alloys primarily formed NiO, with chromium oxides near the oxide/base alloy interface. In625 exhibited similar corrosion performance in relation to previous tests, lending confidence in comparisons between past and present experiments. HA230 exhibited internal oxidation that consisted of a nickel/chromium oxide. Alloys with significant aluminum alloying tended to exhibit superior performance, due formation of a thin alumina layer. Soluble corrosion products of chromium, molybdenum, and tungsten were also formed and are thought to be a significant factor in alloy performance.

ACKNOWLEDGMENTS

Authors would like to gratefully acknowledge the metallography preparation and analysis of Ryan Nishimoto and Andrew Gardea, with electron microprobe analysis of Miles Clift. Review, discussions, and insightful comments of Robert Bradshaw were helpful in understanding previous efforts in testing of this nature and interpreting results.

Sandia National Laboratories is a multi-program laboratory managed and operated by Sandia Corporation, a wholly owned subsidiary of Lockheed Martin Corporation, for the U.S. Department of Energy's National Nuclear Security Administration under contract DE-AC04-94AL85000

CONTENTS

FIGURES

TABLES

NOMENCLATURE

ATI	ATI Allegheny Ludlum
BO	Base metal oxide
BSE	Back Scatter Electron Image
CTE	Coefficient of Thermal Expansion
EDS	Energy dispersive spectroscopy
G	Gibb's free energy
HA	Haynes Alloy
IN	Inconel Alloy
M"	Mass normalized by surface area (mg/cm^2)
sCO_2	Supercritical carbon dioxide
SEM	Scanning Electron Microscopy
SEI	Secondary Electron Image
SNL	Sandia National Laboratories
SO	solute oxide
SS	Stainless Steel
X	Oxide thickness
XRD	X-ray diffraction
WDS	Wavelength Dispersive Spectroscopy
$\Delta_f G°$	Gibb's free energy of formation

1. INTRODUCTION

Concentrating solar power (CSP) seeks to raise power cycle temperature for improved energy efficiency [1],(and other references). The challenge in increasing temperatures is realized in receiver design and thermal energy storage (TES). TES for many plant concepts consist of a two tank system for hot and cold fluids, modeled after experience gained on Solar Two [2, 3]. The hot tank for current plants operate up to 575°C, due to concerns with thermal stability and equilibrium metal oxides present in the melt [4-7]. Thermal stability of salts and its implications in regards to thermo-physical properties (viscosity, density, heat capacity, melting point, etc.) and materials corrosion of receivers and hot tanks are still of concern.

Numerous studies have been done in the past at Sandia National Laboratories (SNL) with particular emphasis on a limited number of high temperature alloys (316SS, Alloy 800, In625, In718) [6-9] under typical operating conditions with variations in salt purity, specifically chloride content. The desire in this study was to test a spectrum various alloys at 600°C, which is the highest operating temperature currently advised for binary solar nitrate salts [10, 11]. The goal of this study was to compare alloys with less nickel content to high nickel alloys, such as In625. This test evaluated thirteen alloys (Table 1) establishing relative performances between alloys. In addition to corrosion rates up to 3000 hours, a standard suite of metallographic analysis was used to determine corrosion products formed during tests.

Page intentionally left blank

2. EXPERIMENTAL METHODS

All corrosion tests were isothermal in nature and fully immersed in the binary nitrate salt. The set up used in this experiment were discussed elsewhere [12]. Samples, obtained from Specialty Metals with 120 grit finish, were suspended on an alloy tree (see Figure 1) with ceramic washers separating samples. The salt was not mechanically agitated during testing; however, air sparging ensured no thermal stratification occurred during testing.

Table 1: Alloy compositions used during corrosion study

	Cr	Mo	Ni	Mn	Si	Fe	Co	W	Al	Other
321SS†[a]	17.28	0.34	9.10	1.80	0.63	70.37	-	-	-	Cu (0.32), Ti (0.16)
347SS† [a]	17.45	0.32	9.43	1.57	0.63	69.72	-	-	-	Nb (0.62 max), Cu (0.26 max)
253MA* [a]	20-22	-	10-12	0.8	1.4-2	63-68	-	-	-	Ce (0.08 max), N(0.20 max)
HA556† [b]	21.44	2.02	21.04	0.93	0.37	32.58	18.43	2.30	0.15	Zr(0.01), Ta(0.73)
RA330* [a]	18-20	-	34-37	2	1-1.5	38-44	-	-	-	Cu(1.0 max)
S35140 * [a] (ATI20-25)	20-22	1-2	25-27	1-3	0.75	44-52	-	-	-	Nb(0.75 max)
ATI332Mo* [a]	21	2.4	34.5	1.1	0.4	40.2	-	-	-	Nb(0.4 max)
HR224† [b]	20.50	0.21	46.44	0.33	0.31	27.62	0.38	-	3.86	Ti(0.35)
HR120† [b]	24.91	0.27	37	0.68	0.50	36.41	0.15	-	0.08	
HA230† [b]	22.37	1.27	59.41	0.49	0.42	1.32	0.19	14.16	0.32	Cu(0.05)
HA242† [b]	8.05	24.79	65.44	0.29	-	1.24	-	-	0.13	Cu(0.06)
In625† [b]	21.76	8.28	61.0	0.21	0.25	4.46	0.08	-	0.20	Nb(3.38), Ti (0.24)
HA214* [b]	16	-	75	0.5	0.2	3	-	-	4.5	Zr(0.1 max)
* nominal compositions of alloys, †actual composition tested from heat a. Vessel 1, b. Vessel 2										

Samples were removed in standard fixed interval testing format [13], where samples were nominally removed at 500, 1000, 2000, and 3000 hours. Limited sample removal motivated testing of a large spectrum of alloys in two testing vessels. Repeat samples (347SS and HA230) indicated that the corrosiveness of the melt did not significantly change over time for the alloys tested. Specific sample configurations and actual pull schedules are in the appendix of this document (see Table 8).

ASTM G1-03 practices were used as the general guide for oxide removal techniques [14]. The tenacious oxide formed on high nickel content alloys were not easily removed using mechanical or chemical techniques alone. Thusly, combinations of both methods were employed.

Excess salt was removed from the samples prior to oxide removal. Samples were placed in deionized water and cleaned via bath ultrasonication for ten minutes or until the samples appeared visually clear of deposits. Samples masses, with the oxide layer intact, were measured.

Stainless steel alloys used ASTM G1-03 Designation C.7.4 for oxide removal guidance [14]. Samples were washed for five minutes in a boiling $NaOH/KMnO_4$ bath, rinsed for one minute in a room temperature diammonium citrate ($(NH_4)_2HC_6H_5O_7$) bath, and rinsed with deionized water. They were dried with lint free

cotton wipes, weighed, and the process was repeated for a total of four bath cycles. This proved to remove oxide layers satisfactorily.

Oxide layers on nickel based alloys were especially tenacious. Previous attempts, as guided by the ASTM method, to chemically remove the oxide layer were ineffective. Therefore, a modification of the stainless steel method was developed for nickel alloys. Samples were washed for an hour in boiling $NaOH/KMnO_4$ bath, then washed for an additional hour in a boiling diammonium citrate bath, and finally rinsed with deionized water. Samples were dried with lint free cotton wipes and weighed. All samples were then abraded using glass beads, grit 60, until the oxide layer was completely removed. All corrosion samples were compared to pristine base samples, which were also subjected to chemical baths and abrasion to determine if the mass loss was strictly due to the loss of the oxide layer.

Figure 1: Samples attached to tree during molten salt exposure.

X-ray diffraction (XRD) employed the PANalytical Empyrean, located at SNL. Typical 2θ and goniometer methods were used on alloys with thick, dense oxides (such as nickel oxide) allowed excellent detection of the surface corrosion phase. Alloys with thin or less dense corrosion products, such as hematite or magnetite, proved more difficult to measure. Grazing XRD and powder diffraction techniques were employed to detect surface phases.

Scanning electron microscopy (SEM) and energy dispersive spectroscopy (EDS) were performed on the JEOL JSM 840A, with the EDS system from Thermo Electron Corp. All plan and x ray mapping analysis were performed on this instrument.

3. RESULTS AND DISCUSSION

A. Molten Salt Analysis

Previous work suggested that above 577°C that oxide concentrations are below 1% (molar) [4] and, for practical purposes, the stability of solar salt is limited to 600°C [5]. Despite this expected stability, a wide spectrum of inorganic analysis was carried out to determine any anomalous behavior and to determine potentially soluble products.

Solidified salt transited in color from white (0 hours) to yellow (2000 hours) to green (3000 and 4000 hours) as shown in Figure 2. The yellow color is typical and has been suggested as a mixture of chromates [15-17], where some of the chromates have been reported to be yellow-green in color [17]. Quantitative assessment of chromium concentration between vessel one and two, Figure 4, provides evidence that the amount of chromium in the melt is proportional to relative concentrations found in alloys. Vessel two had more chromium rich alloys when compared to vessel one.

Figure 2: Salt color at 2000 hours (left) and 3000 hours (right).

Nitrite concentration has been monitored in past experiments due to the expectation that nitrite tended to decompose into various products (i.e. N_2, O_2, NO_x, or oxide) [18-20]. High oxide content, also called melt alkalinity, exacerbates corrosion through interactions with the container alloys and is a critical parameter. Unfortunately, it is difficult to measure oxide content explicitly and use of the following reaction was suggested to determine equilibrium [21]:

$$\boldsymbol{O^{2-} + H_2O \rightleftharpoons 2OH^-} \qquad \text{Equation 1}$$

Measurements were attempted in this test, but were unreliable and largely scattered. Due to this result, attempts to interpret results based on oxide content were abandoned during this study. Determination of melt alkalinity is highly recommended for research and development in future studies, as this data is thought to better correlate corrosion performance.

Nitrite/nitrate, chloride, sulfate, and carbonate behavior were very similar between the two corrosion vessels. NO_2/ NO_3 equilibrium measurements in this study were compared to equilibrium calculations[11, 22] and were found to be about three percent higher than values determined from previous experiments [7], as depicted in Figure 3. Equilibrium calculations assumed the salt temperature to be 600°C, with an oxygen partial pressure of 0.17 atm, due to the elevation in Albuquerque, New Mexico. While NO_2/ NO_3 values were higher than expected, comparisons between vessels were effectively equivalent. Analysis was performed at McCampbell Analytical using various techniques (E300.0, SW6010B, SW6020, SM5310B, SM2320B).

Chloride content was low as specified in the salt grade, approximately 500ppm (shown in Table 2), for the duration of the experiment. Carbonate content increased during the experiment due to the reaction of carbon dioxide with oxide in the melt. This was expected as no precautions were taken to scrub CO_2 from the inlet air stream. This parameter simulated expected plant conditions.

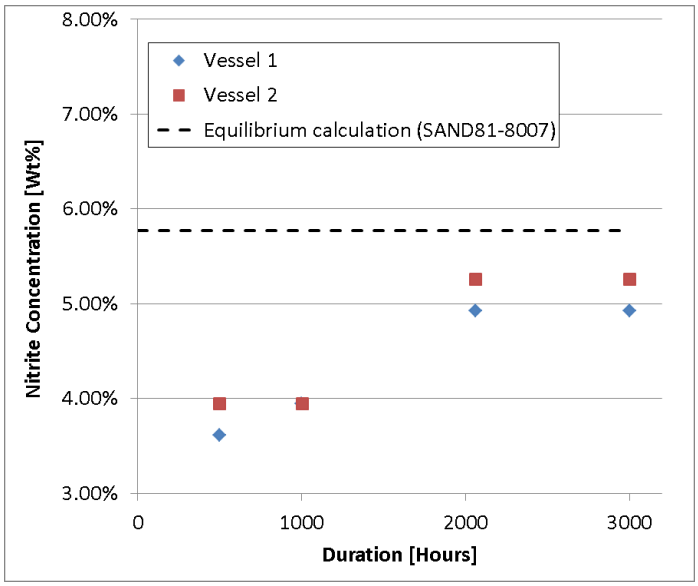

Figure 3: Nitrite concentration over time. Calculation performed at 600°C at 0.17atm PO_2.

Table 2: Inorganic impurity concentrations (in wt%) measured over the duration of experiment.

	Pot 1 [time in hours]					Pot 2 [time in hours]				
	0	500	1000	2000	3000	0	500	1000	2000	3000
Impurity										
Chloride*	.053%	0.056%	0.057%	0.058%	0.057%	0.059%	0.058%	0.059%	0.059%	0.058%
Sulfate*	0.15%	0.13%	0.13%	0.12%	0.14%	0.14%	0.14%	0.14%	0.12%	0.12%
Carbonate*	-	0.08%	0.21%	0.25%	0.33%	-	0.20%	0.37%	0.28%	0.36%
* Determined using E300.0										

Dissolved metal analysis was performed on salt melts from each vessel. Since each vessel had substantially different alloys, indicated in Table 1, it was observed that vessel two had substantially more tungsten accumulation over the course of the test (Figure 4), due to Haynes 230 (14% W by weight) and Haynes 556 (2.3% W). Previous work detected WO_4^{2-} which dissolved from tungsten oxide in KNO_3 above 550°C after prolonged heating [23, 24].

Due to the interval testing approach taken in this experiment it is not possible to quantitatively assess behavior (linear vs. parabolic accumulation of soluble products), but interesting qualitative results can be discussed. By inspection, nearly an equivalent weight of elemental tungsten and molybdenum were in contact with the binary salt (approximately 30-40g total of each), due to the relative alloying concentrations in alloys. Figure 4 indicates that tungsten was detected in higher concentration then molybdenum, which may be due to protective oxide barriers formed on molybdenum rich alloys and will be addressed later.

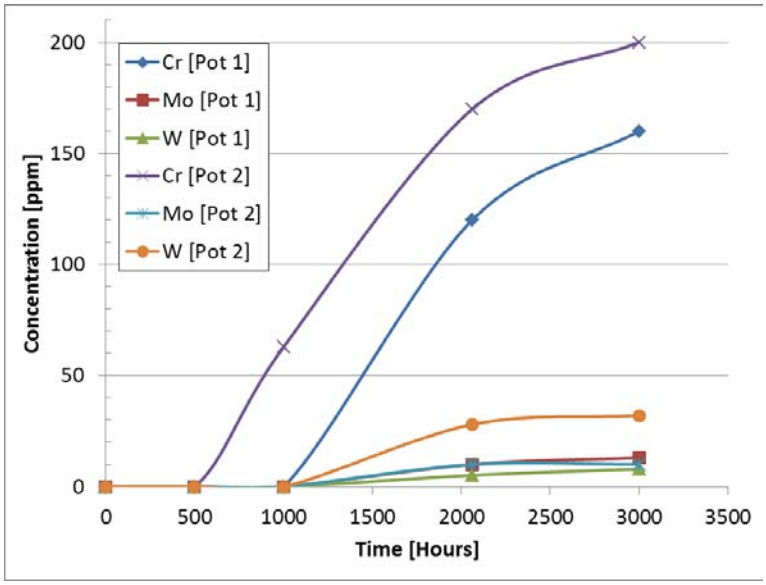

Figure 4: Dissolved metals present in melt. Cr is only detected in concentrations higher than 50ppm. No Ni, Ti were detected (resolved down to 1ppm)

B. Alloy Corrosion Analysis

The weight change and descaled weight loss of exposed samples were investigated. The data analysis is as follows: first, a linear least squares fit was performed on a log-log plot to determine the exponential time dependent behavior, an example of this is in Figure 5. Once the exponential component is set, the value for growth rate can be determined as given in the following equation:

$$\frac{X}{\rho_a} = \Delta M'' = k(t)^n \qquad \text{Equation 2}$$

Where ρ_a is the alloy density, X is the depth of the affected alloy, $\Delta M''$is the area normalized mass loss normalized, t is time (in seconds), k and n are coefficients to be fit.

Calculations to assess corrosion damage were performed as depicted in various standards [13, 14] using the following equation:

$$\frac{\mu m}{yr} = \frac{87600(\Delta M'')}{\rho T} \qquad \text{Equation 3}$$

ρ is alloy density (g/cm^3) and T time hours.

The alloys investigated have been sorted into several sections primarily by the main elemental constituents. An attempt was made to make relevant comparisons in each section using relevant weight gain, descaled loss (corrosion rate), electron microscopy and XRD collocated along with any pertinent discussion.

Sections are as follows:

Fe-Cr-Ni:
321SS [70.4Fe-17.3Cr-9.1Ni], **347SS** [69.7Fe-17.5Cr-9.4Ni], and **253MA** [68Fe-20Cr-10Ni]: **HA556** [32.6Fe-21.4Cr-21Ni -18.4Co] *included for comparison*

Fe-Ni-Cr: **RA330** [41Fe-35.5Ni-19Cr], **ATI20-25Nb** [48Fe-26Ni-21Cr], **ATI332Mo** [40.2Fe-34.5Ni-21Cr] : **HA556** [32.6Fe-21.4Cr-21Ni -18.4Co] *included for comparison*

Ni-Fe-Cr: **HR120** [37Ni-36.4Fe-24.9Cr], **HR224** [46.4Ni-27.6Fe-20.5Cr-3.9Al]

Ni-Mo/Cr: **HA230** [59.4Ni-22.4Cr-14.2W], **HA214** [75Ni-16Cr-4.5Al], **In625** [61Ni-21.8Cr-8.3Mo], **HA242** [65.4Ni-24.8Mo-8.1Cr]

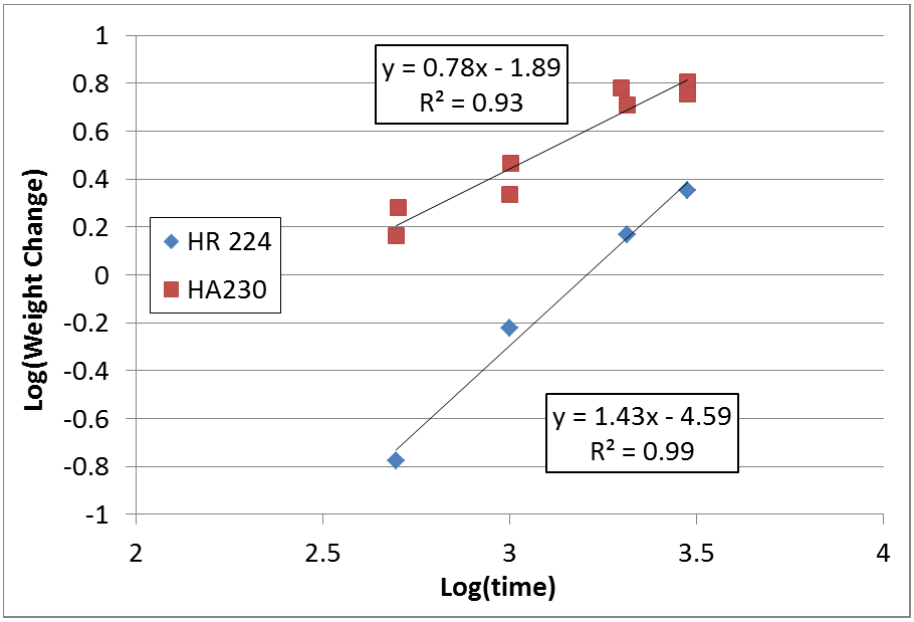

Figure 5: Example fitting technique used to determine scale growth kinetics of descaled weight loss data

i. [Fe-Cr-Ni Alloys]

Alloys of Fe-Cr-Ni tended to form similar oxidation morphologies during testing with a thin layer of $NaFeO_2$ on the outermost layer of 321SS, 347SS, and 253MA as observed in plan view SEM images (Figure 9, Figure 7, Figure 11). Thick inner layers of iron oxide were found directly beneath sodium ferrite with a relatively thin layer of mixed chromium/iron oxide beneath typically adjacent to the alloy (see Figure 10, Figure 8, and Figure

12). The morphology of 321SS, 347SS, and 253MA are in good agreement to previous studies performed on 316SS, an alloy of similar composition [9, 25, 26].

Weight gain information, Figure 6, indicated that the alloy with thickest corrosion product was 253MA, which was further confirmed by cross sectional analysis (Figure 12), and that apparent oxide spallation occurred with 321SS. Obvious regions of delamination and spalling in 321SS with further evidence in plan view images in Figure 9. 321SS surface oxide exhibited poor adhesion in general, as flaking occurred during typical handling. Spallation was reported at higher temperatures (800-1000°) in oxygen environments, where studies found that oxides tended to spall upon cooling, due to stresses arising from the CTE mismatch of the alloy and oxides, and are thought to apply to these observations [27]. Surface cracking in 253MA (Figure 11) was found present after only 1000 hours of exposure, while HA556 exhibited some indication of spalling found in the weight gain data. Error bars associated with 347SS are the result of duplicates samples that were done to determine repeatability. No obvious spallation was apparent with the 347SS alloy.

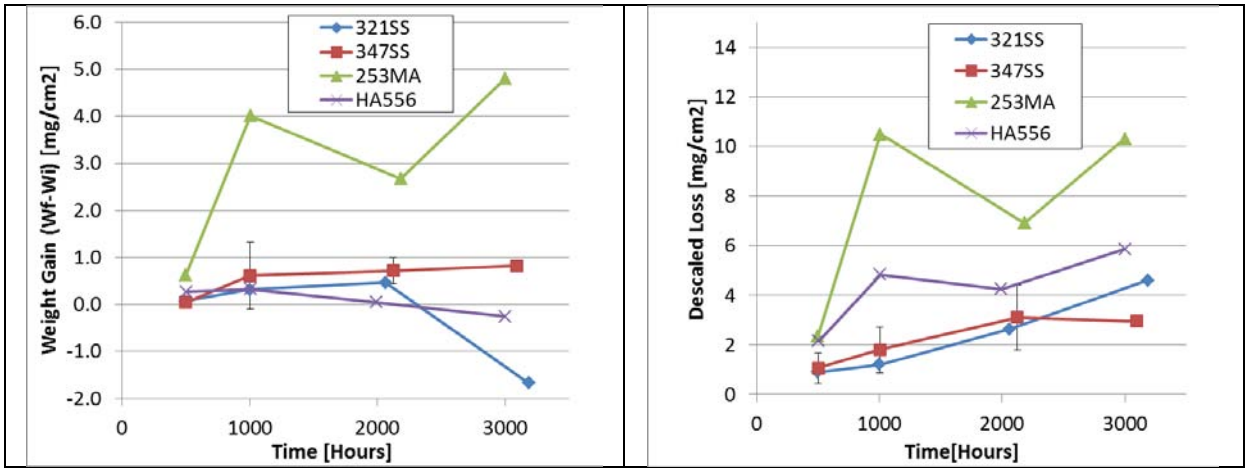

Figure 6: Weight gain data from on Fe-Cr-Ni alloys (left) and descaled data (right). Error bars on 347SS were from duplicate samples taken during the fixed interval test.

Table 3: Corrosion Rates and projections for Fe-Cr-Ni alloys

Alloy	Alloy Density [g/cm^3]	Exponent Fit (n)	k [mg/ cm^2-sec^n]	Descaled Loss* [mg/cm^2]	Metal Loss* [µm/yr]
321SS	7.94	0.89	2.4e-6	4.59	15.9
347SS	8.03	0.6	1.76e-4	2.95	10.4
253MA	7.8	0.8	2.31e-5	10.31	38.6
HA556	8.23	0.48	2.20e-3	5.9	20.8
*Based off of 3000 hour data (Equation 3).					

Assessment of parabolic versus linear oxidation was difficult to interpret with the limited number of time steps sampled during this test. This fact was further convoluted by early stage oxidation, which is expected to proceed as linear rates until the oxide is adequately thick [13]. Despite this limitation, some trends appeared among alloys. 347SS and 321SS, which have the most similar composition of the Fe-Cr-Ni alloys showed the best performance after 3000 hours, even when considering 321SS tendency for spallation. HA556 had similar loss in respect to 321SS, while 253MA was found to be most corroded. Overall corrosion rates are in Table 3 and all alloys exhibit outstanding to excellent corrosion resistance [13].

The fitting coefficient *n* can provide insight into the physical mechanisms that are occurring on the surface. It is clear from the results that 321SS and 253MA both behave in linear fashion, which is indicative of a lack of stable and adherent passive layers. This behavior is contrasted to similar a similar alloy 347SS, and more exotic HA556, where *n*~0.5 and resembles parabolic behavior, and is characteristic of a diffusion limited passive layer. Extrapolating to long times, 347SS and HA556 appear to perform in similar fashions although their respective corrosion morphologies are distinctly different.

347SS was found to have three primary layers: sodium ferrite ($NaFeO_2$), mixed oxides of sodium, iron, nickel and chromium, and Fe_2O_3. $NaFeO_2$ and Fe_2O_3 phases were identified using XRD (Figure 8), while WDS/EDS (See Appendix, Figure 42) provided evidence of several mixed oxides. Formation of a sodium ferrite with mixed oxides were observed for a similar stainless steel (316SS) [9] in previous work, however, it was for higher temperatures (>605°C). Strong similarities were observed between 321SS and 347SS corrosion morphologies and this fact was correlated to empirical corrosion data.

253MA showed the worst performance of the Fe-Ni-Cr alloys. Given the strong similarity of this alloy to 321SS/347SS the discrepancy in oxidation is unclear. Alloying Ce (0.08%wt max) used results in some changes in corrosion resistance, but needs further investigation to fully understand if that is the critical factor in this system [28, 29].

HA556 had a complex oxidation morphology that developed even after 932 hours (Figure 14). Oxygen was the primary salt reactant that was observed in corrosion products with the base metal (some sodium products were observed, but only at the outer surface). In order to provide some understanding to the corrosion structure oxidation equilibrium calculations were performed using the most abundant alloying elements: Fe, Ni, Cr, Co. Compiled values from literature were used for all reactions, with values for the Gibbs free energy of formation interpolated from tabulated values [30]. The oxidation of magnetite is given as an example in the Appendix.

HA556 had an apparent ternary oxide layers due to the presence of cobalt, shown in Figure 15 . Stoichiometric data indicated an outer layer of cobalt oxide, which is complicated to identify due to the concentration of 25% Co, 10%Na, and 10%Mn (balance oxygen). Neither 2θ nor PXRD was able to adequately identify the surface phase. $NaFeO_2$ was identified using PXRD, with possible a phase of $CoFe_2O_4$. The middle layer is composed of 25% Fe and 8-9at%Na (remaining oxygen), which is suggestive of mixed phases of sodium ferrite and hematite phase in a relative concentration of ~40% $NaFeO_2$, ~60% Fe_2O_3. The innermost layer shows enrichment in Co, while Na content is effectively zero. This indicates that the cation species from the melt is only available to form oxides in the outer regions, while solely oxygen is present in the inner region. The likely species present here are $CoFe_2O_4$, as identified in XRD, and Fe_2O_3, as determined from WDS data.

A transition region from oxide to metallic was observed, as indicated by nickel enrichment and increase in Cr content. Protective oxides may be present in such regions and would block diffusion of oxygen into base metal, resulting in an enhanced diffusion of more active trace alloying elements (i.e. Mo, Mn, Ta). Observations of this behavior literature has been referred to as a "gettering effect" [31] and was found to occur with this alloy in other oxidizing environments [32]. More research is needed to provide a clearer understanding as to the performance of HA556 as temperature increases.

Corrosion rates for Fe-Cr-Ni alloys were found to be low, but lack of time step data made it difficult to confidently ascribe linear vs. parabolic kinetics to alloys tested. 347SS lost the least base metal, while 253MA

lost the most. Both 321SS and 253MA appeared to exhibit time linear corrosion, with 321SS performance due surface oxide spallation. Corrosion products detected were primarily oxides involving iron and sodium, with chromium depletion present throughout the oxidation layer. HA556 exhibited cobalt rich oxides due to the high alloying content of cobalt, which was different from the other alloys investigated.

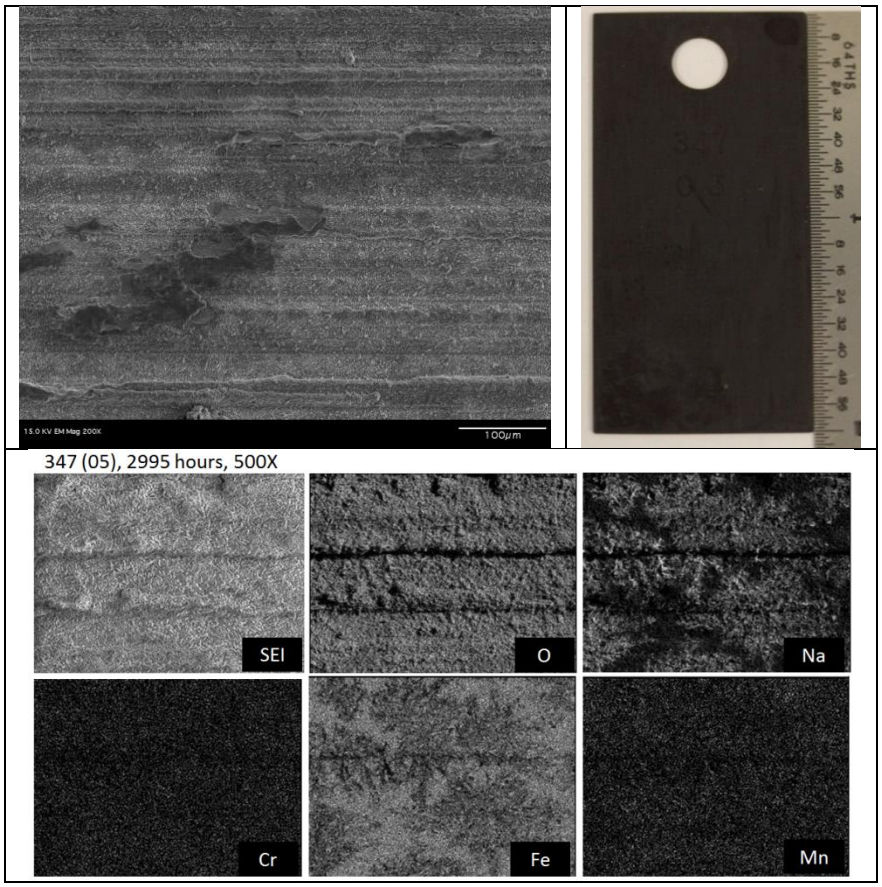

Figure 7: Plan view of 347SS after 1000 hours. Little spallation was observed relative to 321SS. Outermost oxide layer is a sodium ferrite.

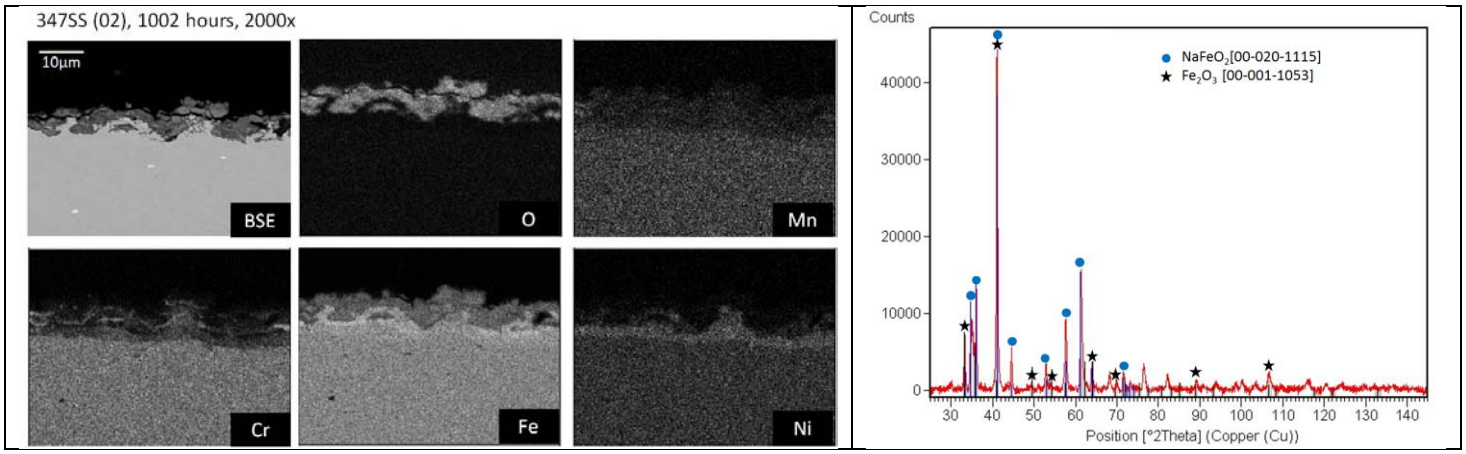

Figure 8: EDS map (left) and XRD data (left) for 347SS

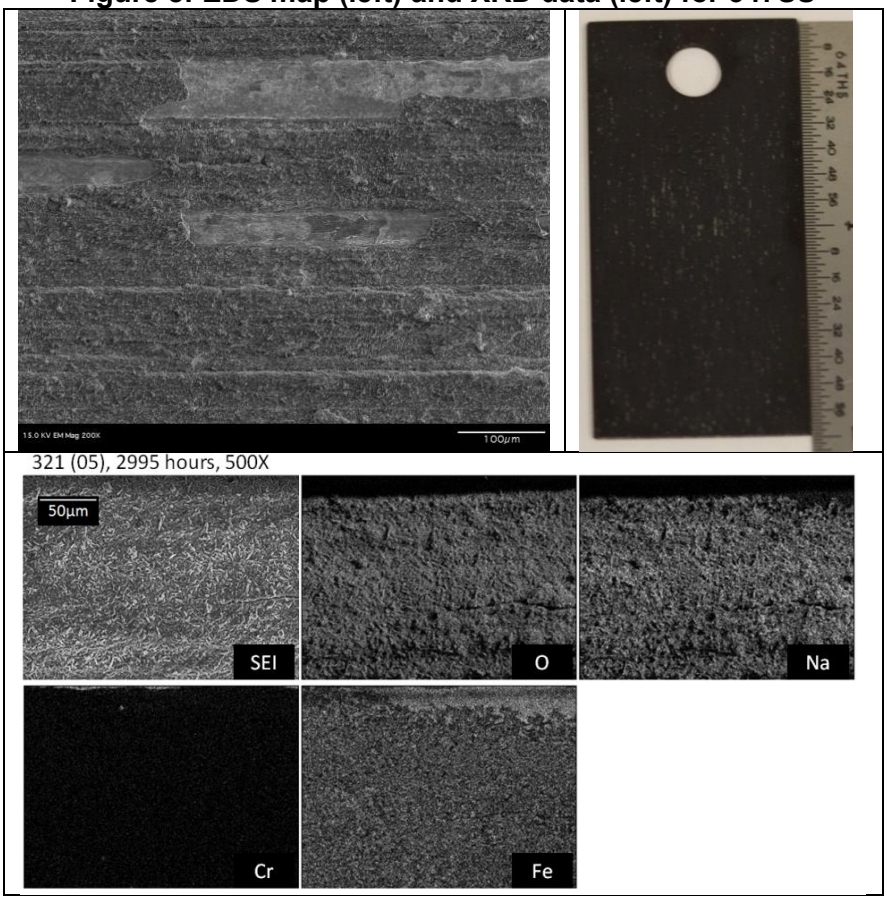

Figure 9: Plan view of 321SS after 1000 hours (top left image). SEM images indicate some spallation present; this was also observed by sparseness of oxide layer in the photo on the right. Outermost oxide is composed of a sodium iron oxide (bottom image).

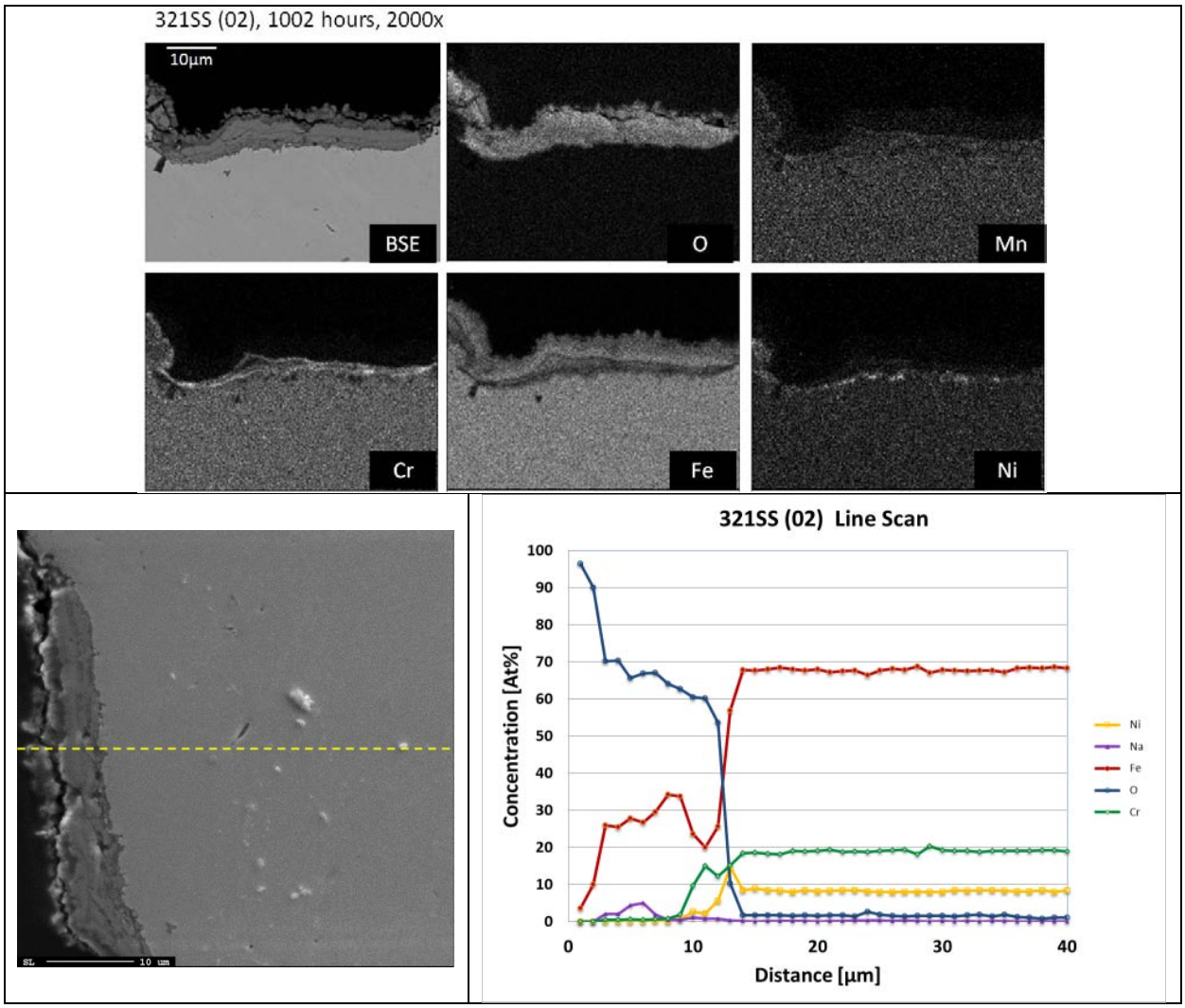

Figure 10: Cross sectional EDS mapping of 321SS with EMP line scan data. Duplex formation of $NaFeO_2$ in contact with the melt and mixed iron, chromium and nickel oxides near base alloy.

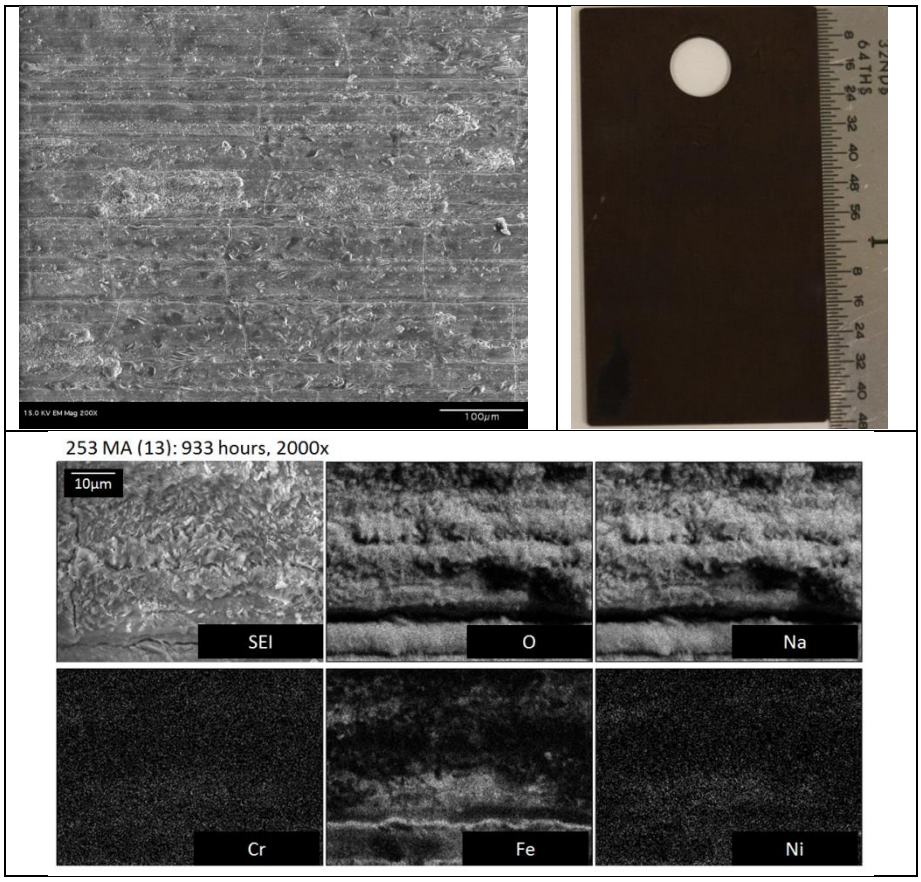

Figure 11: 253MA after 933 hours. Surface cracking (top left) in oxide layers can be observed.

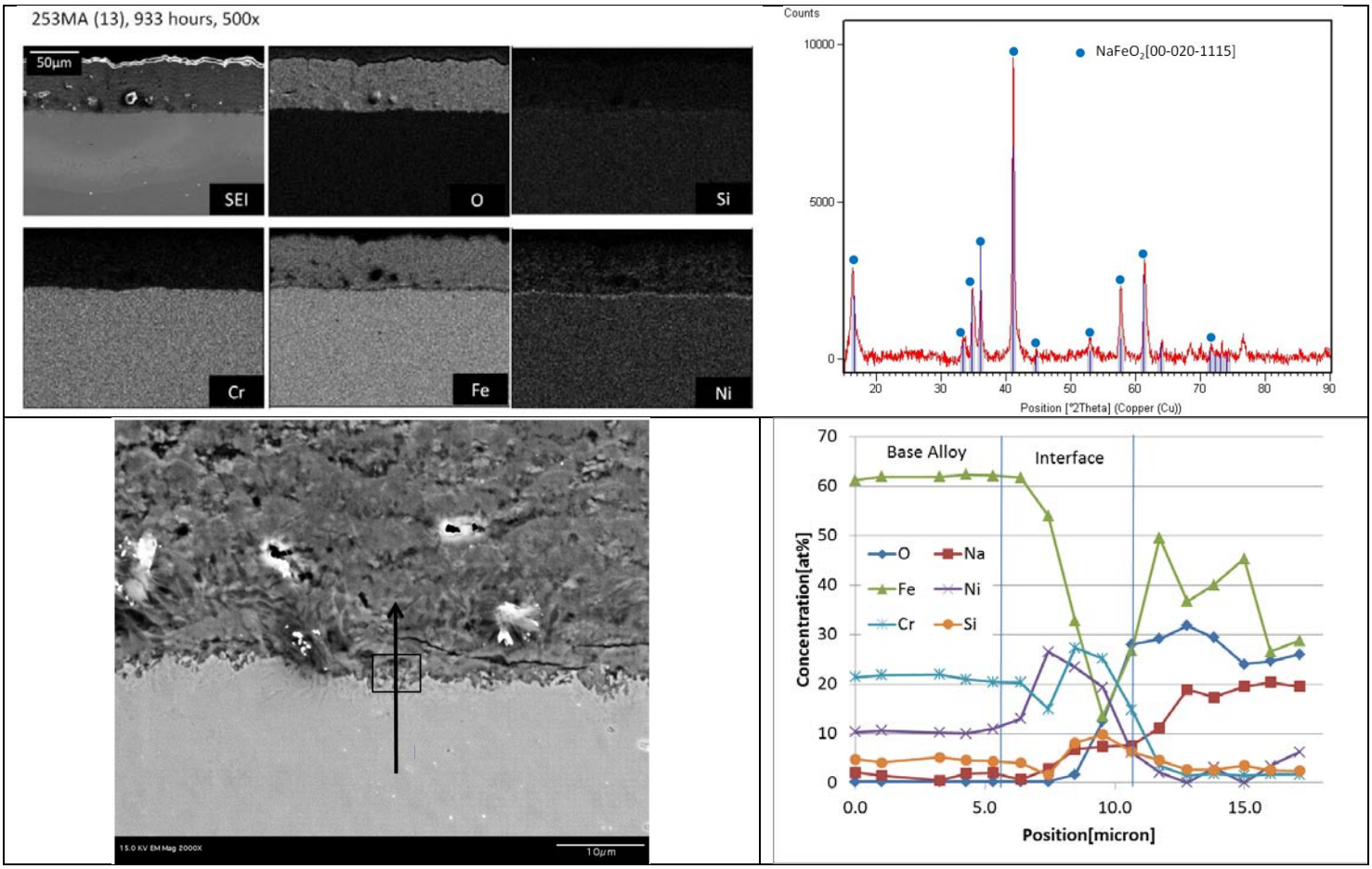

Figure 12: Cross section EDS map of 253MA. Magnified view (bottom left) shows line scan with box depicting interface portion of scan.

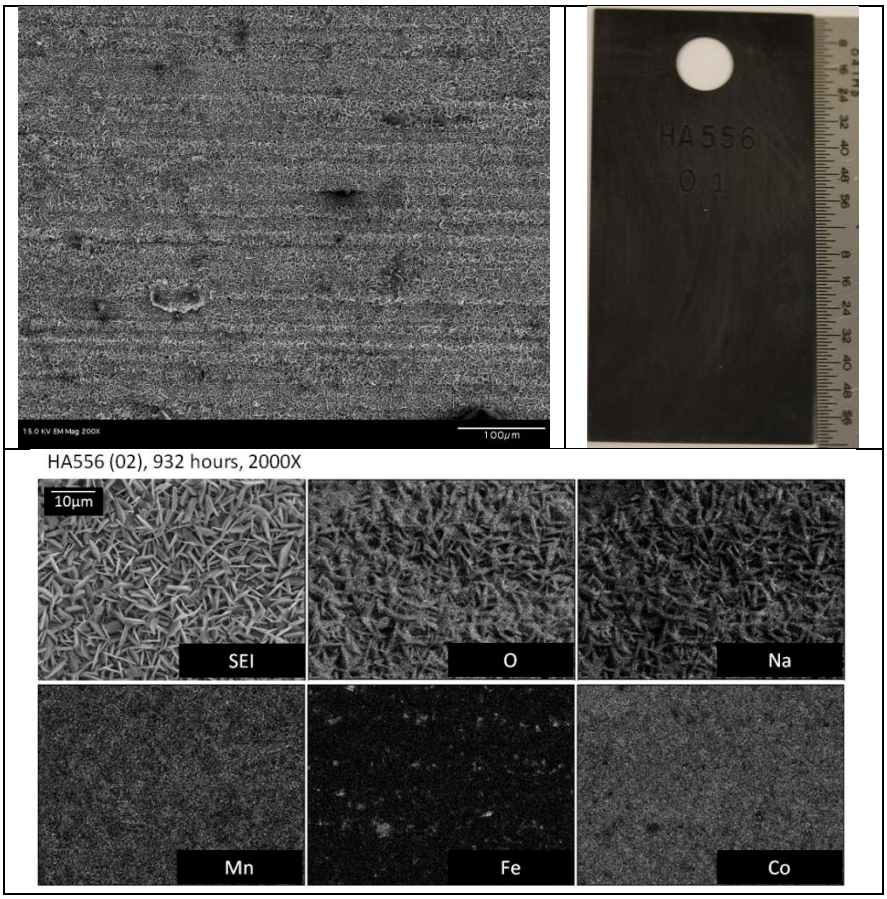

Figure 13: HA556 after 932 hours.

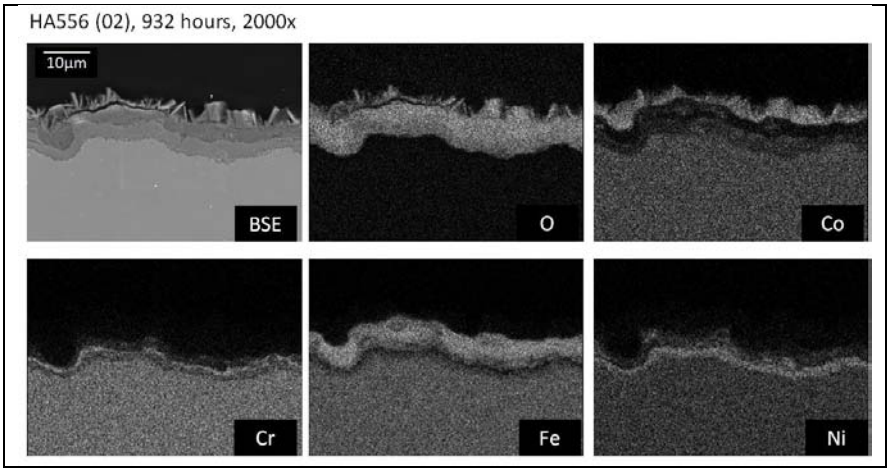

Figure 14: EDS map of HA556 after 932 hours.

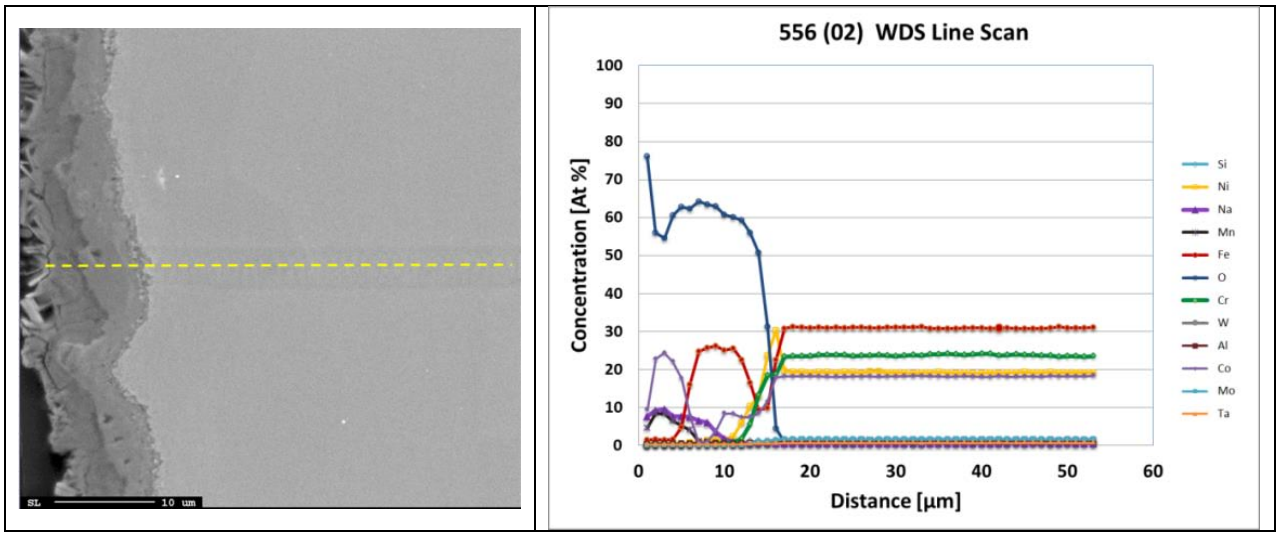

Figure 15: EMP line scan data for HA556 at 932 hours

ii. [Fe-Ni-Cr Alloys]

Fe-Ni-Cr alloys corrosion was uniform and consistent with previous experiments on similar alloys [9]. Corrosion rates after 3000 hours were low, with all alloys less than 21 µm/year when extrapolated linearly from 3000 hour test (Table 4). 332Mo (Fe-34.5Ni-21Cr) and S35140 (Fe-26Ni-21Cr) morphologically similar; thin outer layer of sodium ferrite followed by iron oxide, which gives way to a mixed Fe/Ni oxide. This oxide layer sandwiches an enriched Cr oxide. Alloy 800 (Fe-31Ni-20.7Cr) exhibited similar behavior at 605°C, both in regards to corrosion rate and corrosion product morphology [9].

Weight gain provides insight into oxide adhesion and soluble corrosion products. Net loss may indicate spallation or elemental dissolution, while weight gain typically corresponds to corrosion product accumulation as a result of chemical reactions with the heat transfer fluid. Alloys, with the exception of HA556, gain weight during the test duration. 332Mo and S35140 are exceptionally invariant in mass gain from 1000 hours to 3000 hours (Figure 16). Formation a protective layer appeared rapidly, less than 1000 hours. Weight gain data is reminiscent of a logarithmic rate behavior, however this behavior is typically expected for oxidation below 300-400°C [13, 33].

Austenitic alloys S35140 and 332Mo have the best corrosion performance, followed closely by RA330 and HA556. While overall surface corrosion for all four alloys is regarded as low, given the limited number of data points available, the true nature (linear vs. parabolic, etc.) cannot be asserted with high confidence at this juncture.

332Mo formed a duplex oxide, consisting of sodium ferrite ($NaFeO_2$) and iron oxide phase on the outer surface, followed by mixed oxides of Ni/Fe/Cr on the inner layer, many of which had overlapping peaks in XRD (Figure 18). Depletion of iron and chromium created a transition zone of nickel enrichment that is comparable in thickness to the duplex oxide layer.

S35140 formed a duplex layer similar in nature to 332Mo. The outer layer is again composed of $NaFeO_2$ with phases of mixed oxide. As observed in the EDS point scan (Figure 20) the overall sodium and iron content indicate that $NaFeO_2$ is the primary product on the outermost surface, due to the near equimolar ratios of Na and

Fe. The inner mixed oxide was greatly enriched in chromium and may indicate the transport of chromium through the mixed oxide layer. No depletion zone was detected in S35140 past the oxide/metal interface.

RA330 had a more complicated oxide morphology compared to previously discussed alloys. The oxide depth and nickel enriched zone paralleled behavior observed in 332Mo. However, oxides formed were more complex, as shown in EDS line scan and elemental mapping (Figure 22). Silicon oxide and nickel oxide formed near the oxide/nickel enriched interface that transitioned into mixed products of iron oxide and $NaFeO_2$ on the surface.

The research here indicates all Fe-Ni-Cr alloys are quite corrosion resistant, with metal losses less than 21µm/year after 3000 hours. 332Mo and S35140 exhibit near logarithmic behavior in descaled weight loss, RA330 corrodes linearly with time, and HA556 demonstrates parabolic behavior.

Oxide morphologies vary significantly among alloys. 332Mo and S35140 exhibited duplex structures consisting of mixed oxides and sodium ferrite. HA556 demonstrated a similar oxide structure, with the addition of a cobalt iron oxide on the outer surface. RA330 had complex formations of nickel, iron, chromium and silicon oxides, with a sodium ferrite on the surface.

This section provides initial data, but a more complete set of removal data will establish accurate fitting parameters that can be used for long term extrapolations, as oxide scales may still be evolving even after 3000 hours.

Corrosion rates for Fe-Ni-Cr alloys were found to be somewhat lower than Fe-Cr-Ni, but again, lack of time step data made it difficult to confidently determine the time dependent nature of corrosion (i.e. linear vs. parabolic kinetics). S35140 and 332Mo performed the best over the duration of the test, with asymptotic increase in corrosion after 1000 hours. More data is needed to further assess the performance of these alloys, but initial results are promising. Corrosion products tended to have iron and sodium in layers exposed to salt, while inner oxides were complex mixtures of nickel, chromium and iron. Alloys exhibited nickel enrichment at the oxide/alloy interface consistently.

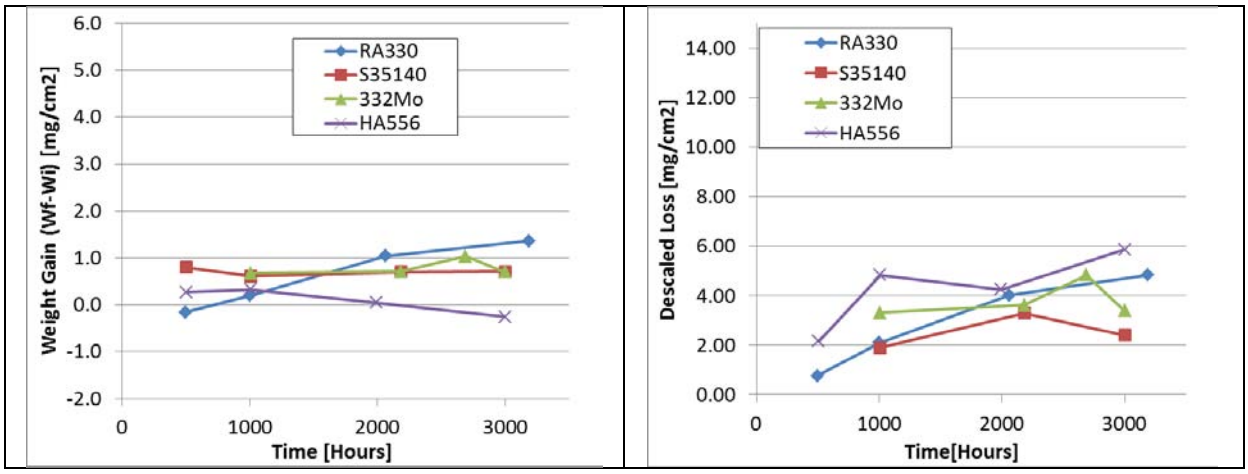

Figure 16: Weight gain information

Table 4: Corrosion rate fitting parameters and extrapolated metal loss per year

Alloy	Alloy Density [g/cm^3]	Exponent Fit (n)	k [mg/ cm^2-sec^n]	Descaled Loss* [mg/cm^2]	Metal Loss* [µm/yr]
RA330	8.22	1.0	3.99e-7	4.8	16.2
S35140	7.96	-	-	2.4	8.8
332Mo	8.13	-	-	3.4	12.2
HA556	8.23	0.48	2.20e-3	5.9	20.8
*Extrapolations to be used for illustrative purposes and based off of 3000 hour data.					

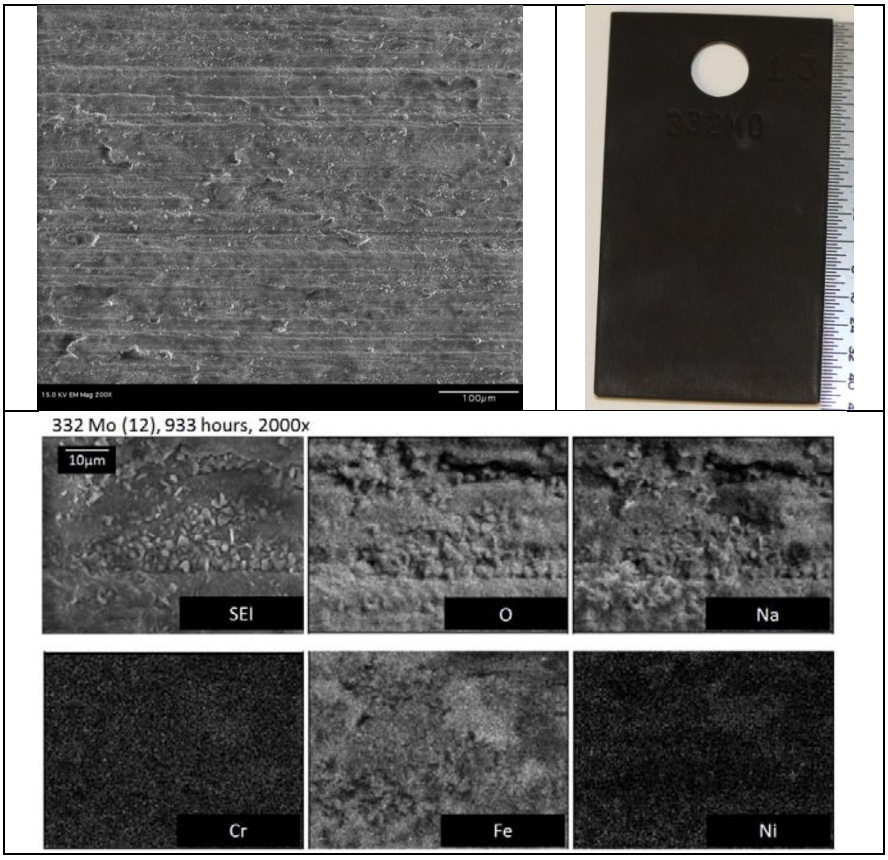

Figure 17: Plan view of 332Mo after 933 hours. No surface cracking was detected

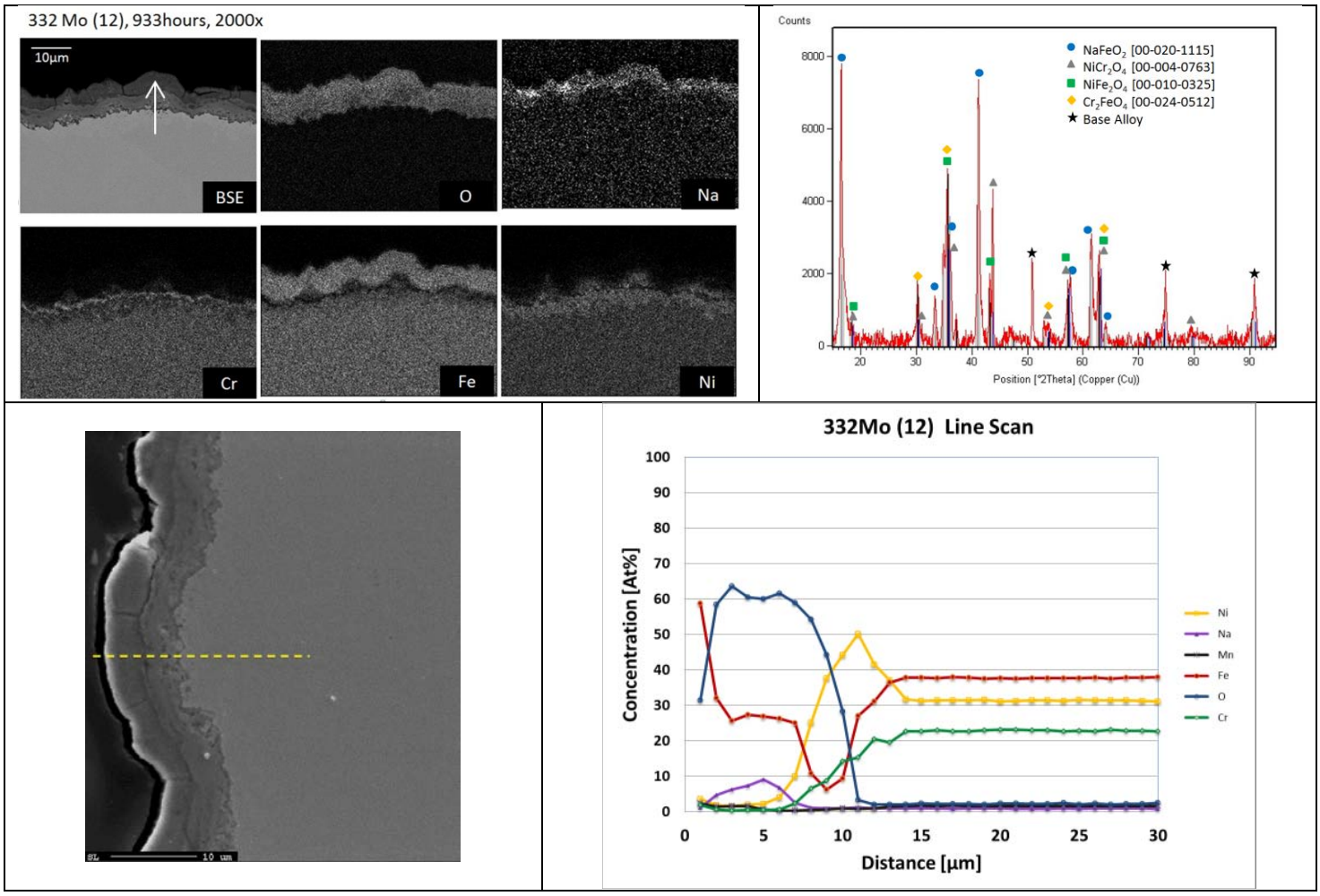

Figure 18: EDS map of oxide found on 332Mo, with representative line scan. Depletion of Fe and Cr was of near equal thickness of oxide region.

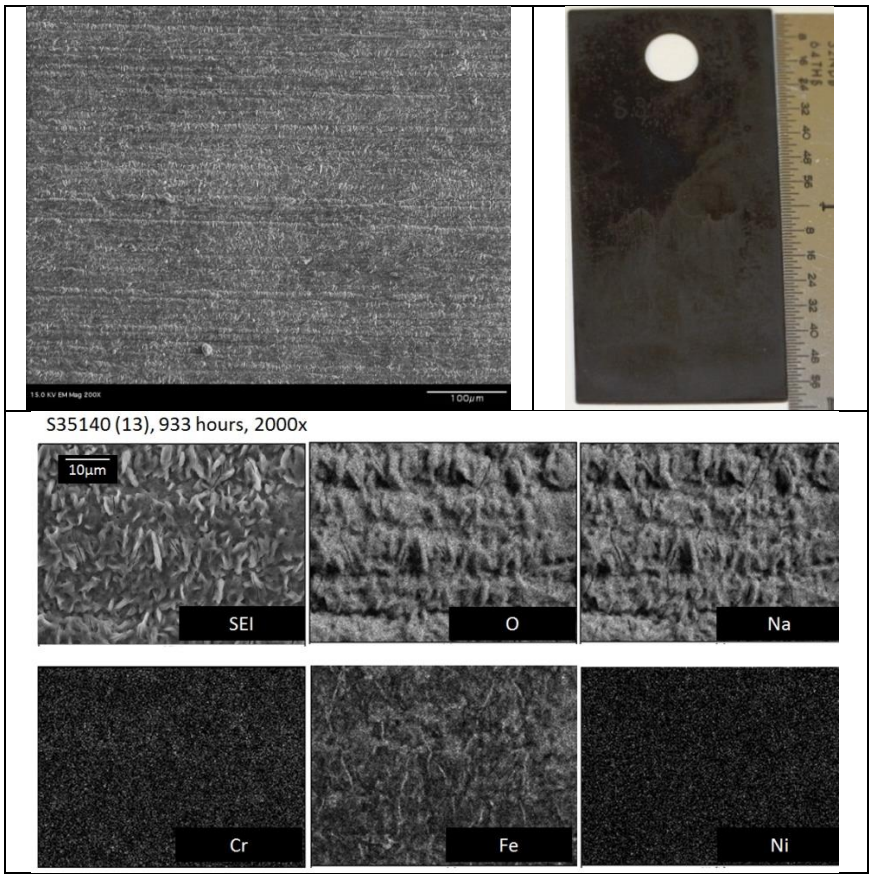

Figure 19: S35140 plan view and photographs after 933 hours

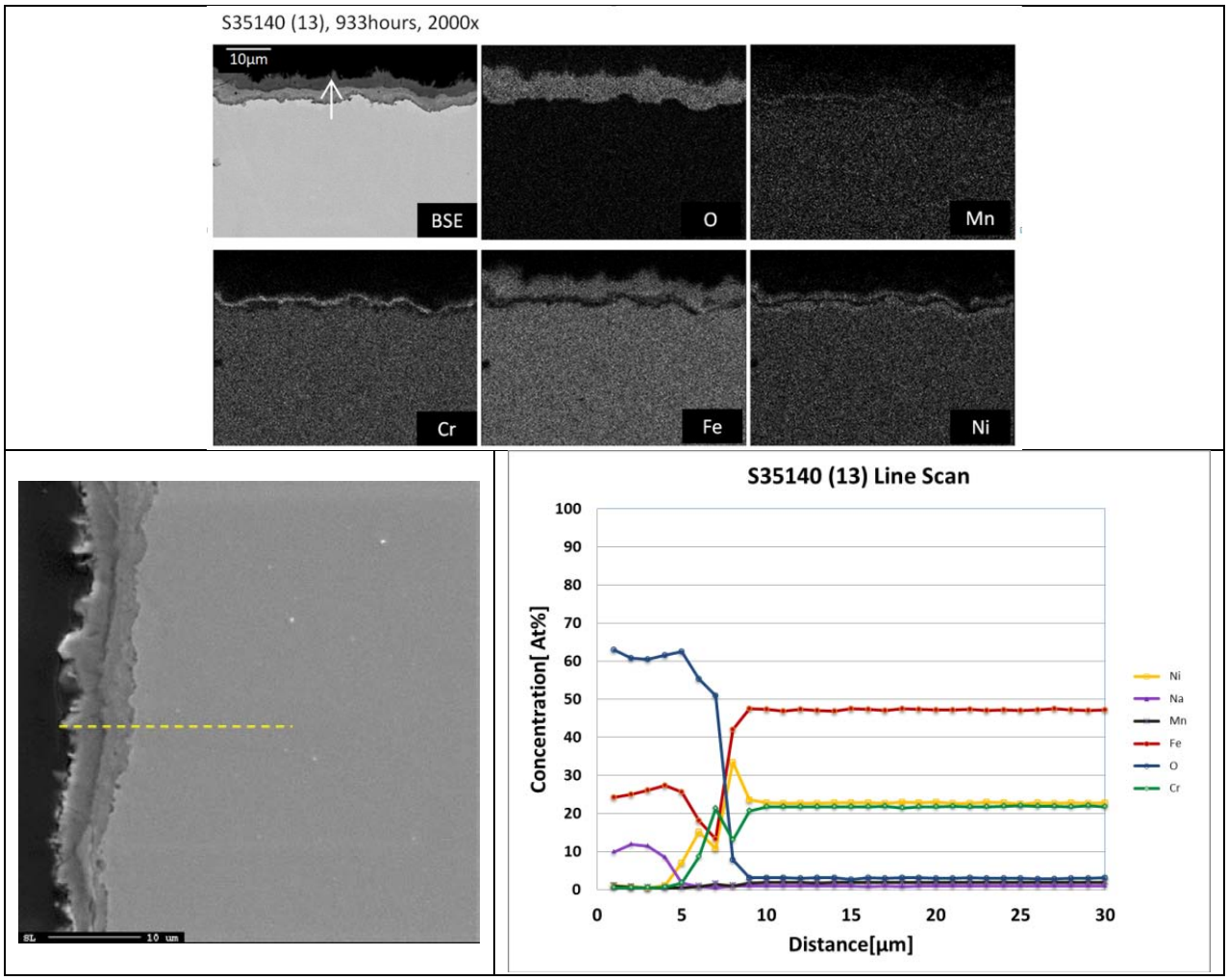

Figure 20: EDS map of oxide found on S35140, with representative EDS line scan. No obvious depletion zone was observed in conjunction to the mixed oxide interface.

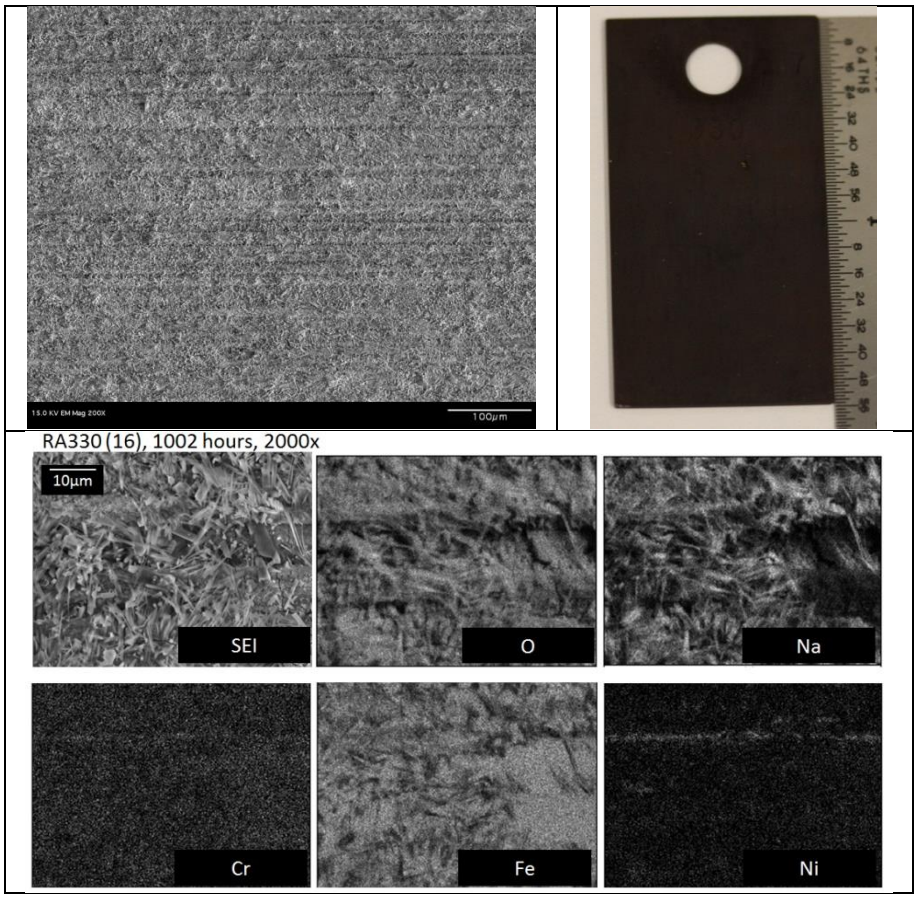

Figure 21: RA330 plan view and photographs after 1002 hours.

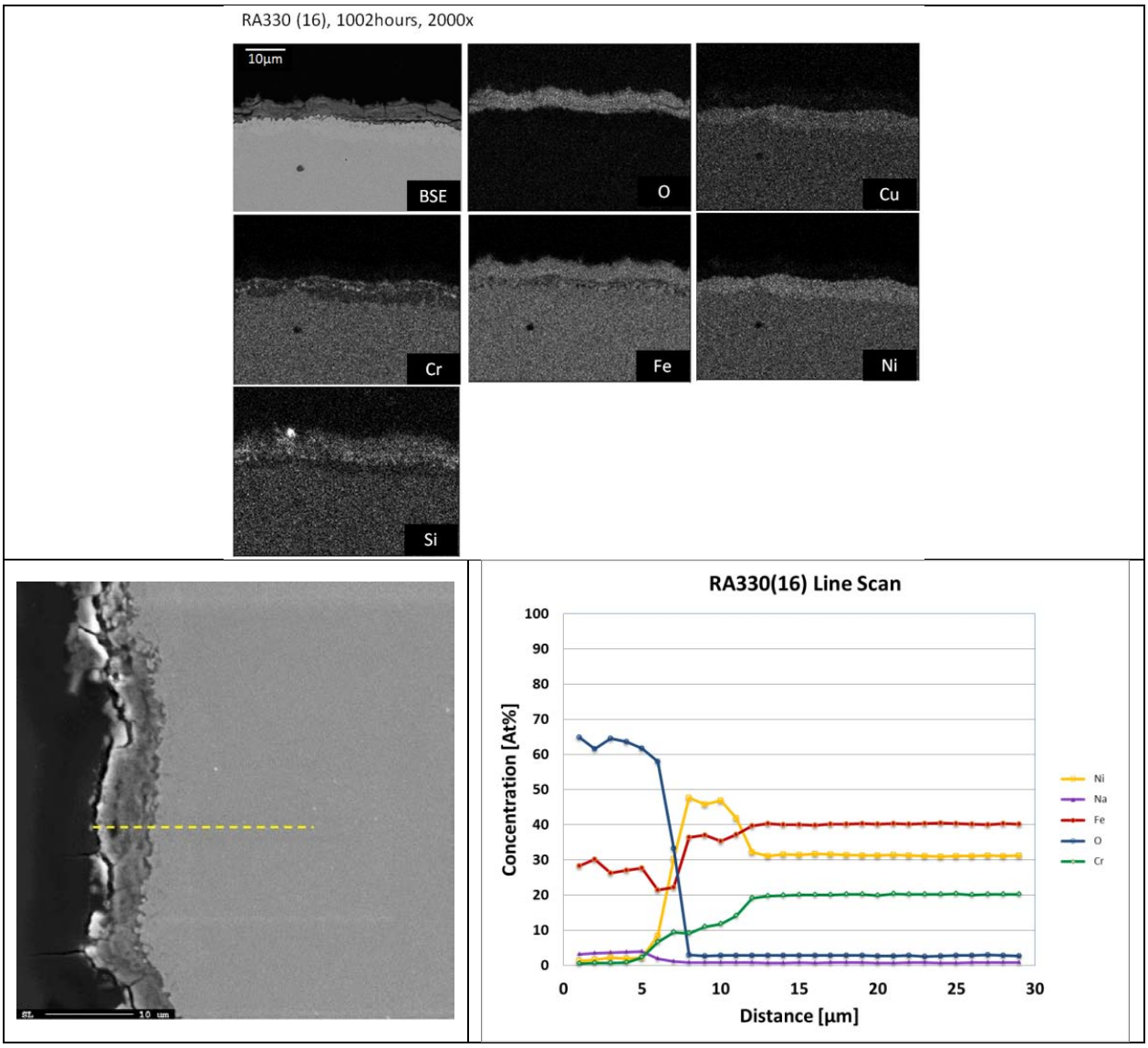

Figure 22: EDS map of oxide on RA330, with representative EDS line scan. Transition (oxide free zone) nearly equivent thickess to oxide depth.

iii. [Ni-Fe-Cr Alloys]

Alloys in this section, which decrease in alloying elements by Ni-Fe-Cr, are similar in composition to the previous section. HR120 exhibited similar behavior to S35140 and 332Mo (both are ATI alloys) in corrosion performance, which make intuitive sense as these alloys are nominally similar (HR120 had slightly higher nickel and chromium content). While the corrosion rate of HR120 was slightly higher than the ATI alloys, asymptotic growth of oxide was observed after 1000 hours. Corrosion products, identified by WDS data, where comparable to the other iron based steels, primarily large amounts of sodium ferrite with mixed oxides of nickel and chromium (Figure 24). One apparent difference is nickel enrichment at the scale/base interface. Backscatter images and EDS mapping (Figure 26) provided some evidence that internal oxidation may be occurring. Oxide stringers observed here were relatively small and may not result in any significant issue. Upon some review of this alloy in other high temperature

oxidizing environments [34], specifically air, HR120 greatly out performed alloy 347SS and S35140. The drastic results may be due to chemistry changes in the oxide layer by depletion of the chromium.

HR-224 showed excellent resistance to oxidation, only rivaled by HA214. There was nearly no weight change over the duration of the test (Figure 23) and surface scale was incomplete. Resistance was attributed to high aluminum content, which was noted in other oxidation experiments [35]. Plan view and cross sectional analysis that surface corrosion products are likely sodium ferrite, as observed in many of the iron based alloys.

Corrosion rates for Ni-Fe-Cr alloys were found similar to Fe-Ni-Cr and, as previously stated, insufficient time step data made it difficult to resolve the time dependent nature of corrosion (i.e. linear vs. parabolic kinetics). HR120 had corrosion morphologies nearly identical to 332Mo, which had comparable concentrations of Ni, Fe, and Cr. HR224 performed very well, with incomplete surface oxidation even after 3000 hours. This fact was ascribed to the high concentration of Al, which would form a protective layer of Al_2O_3.

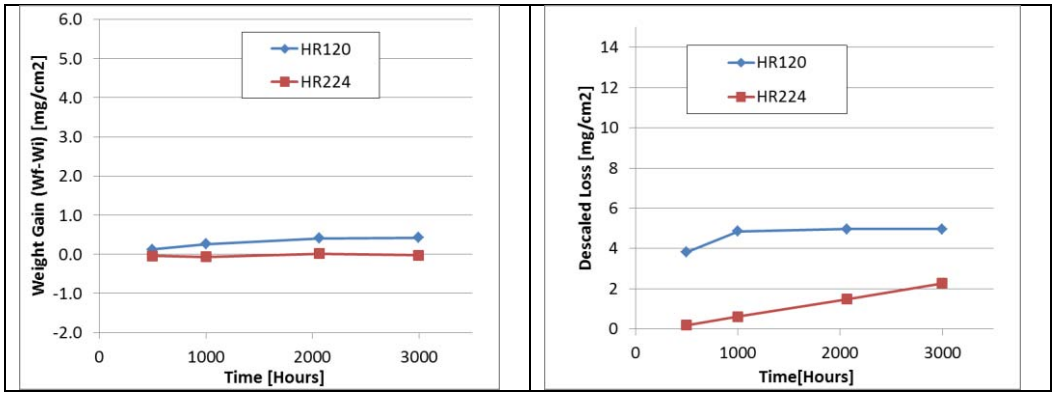

Figure 23: Weight gain and descaled losses during 3000 hour test

Table 5: Corrosion rate fitting parameters and extrapolated metal loss per year

Alloy	Alloy Density [g/cm^3]	Exponent Fit (n)	K [mg/ cm^2-sec^n]	Descaled Loss* [mg/cm^2]	Metal Loss* [µm/yr]
HR120	8.07	0.14	5.03e-1	4.97	18
HR224	8[a]	1.4	4.36e-10	2.27	8.3
*Based off of 3000 hour data (Equation 3) a. No density was found in literature and a density of 8 was assumed					

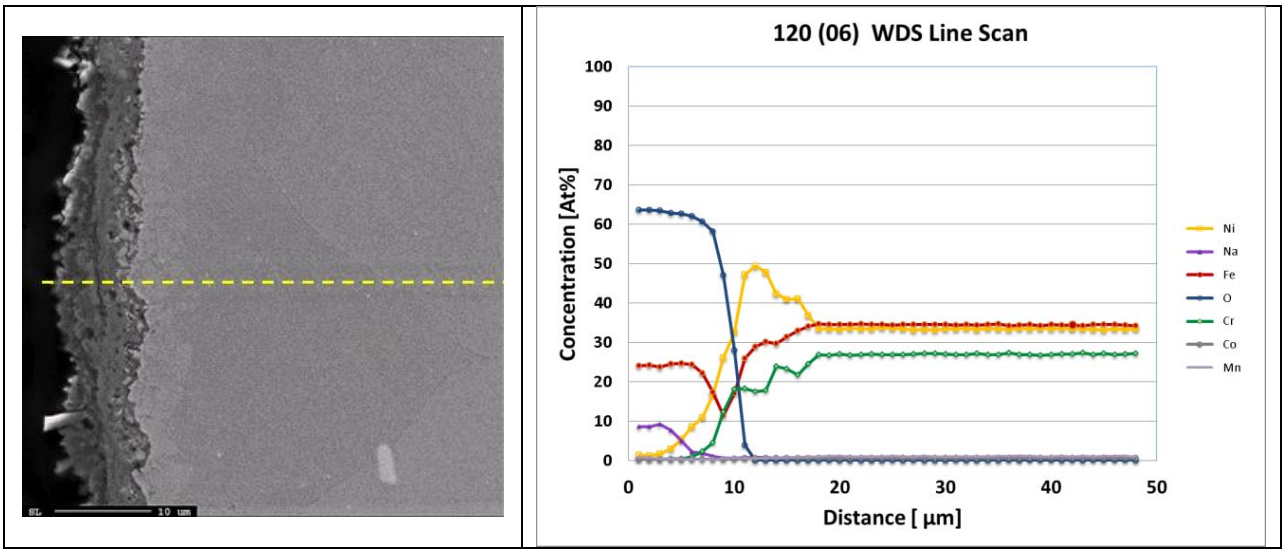

Figure 24: Line scan data of HR120 (2995 hours) indicates that likely mixed oxides (sodium and iron) are present.

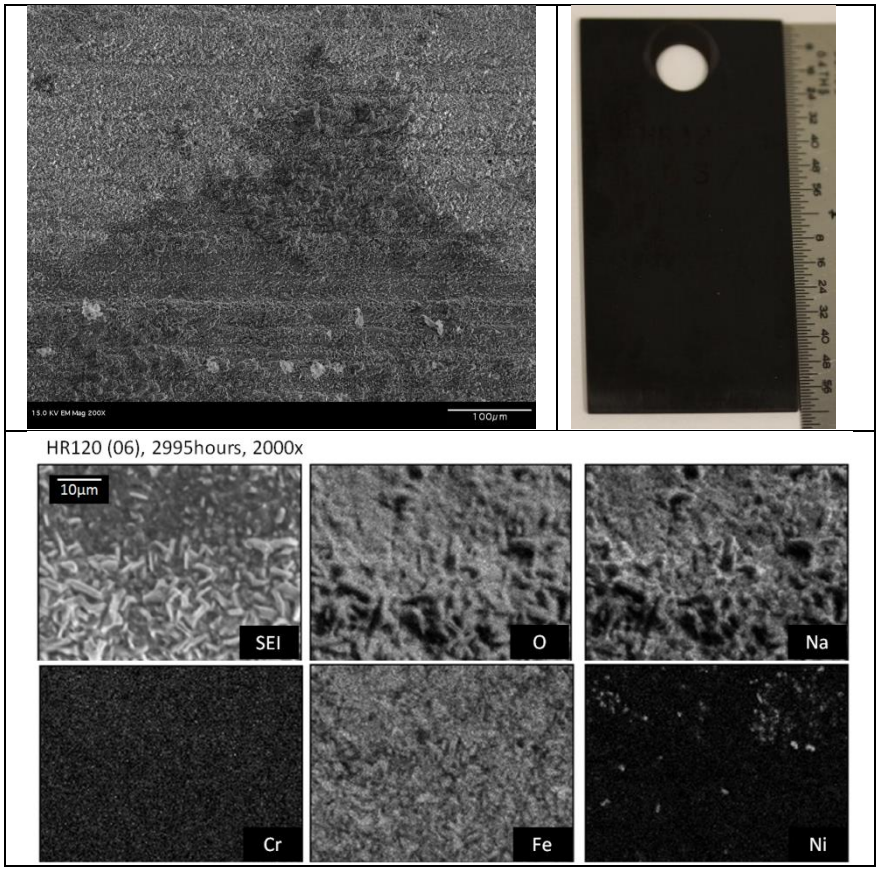

Figure 25: SEI images of 2995 hours exposures.

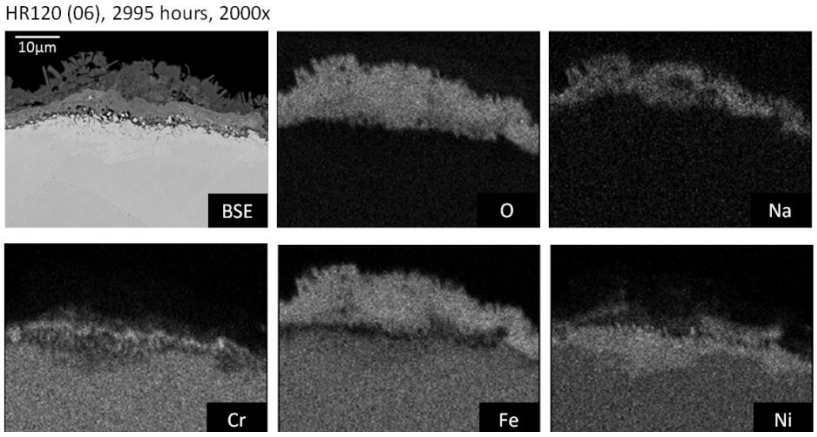

Figure 26: X-ray map of HR120

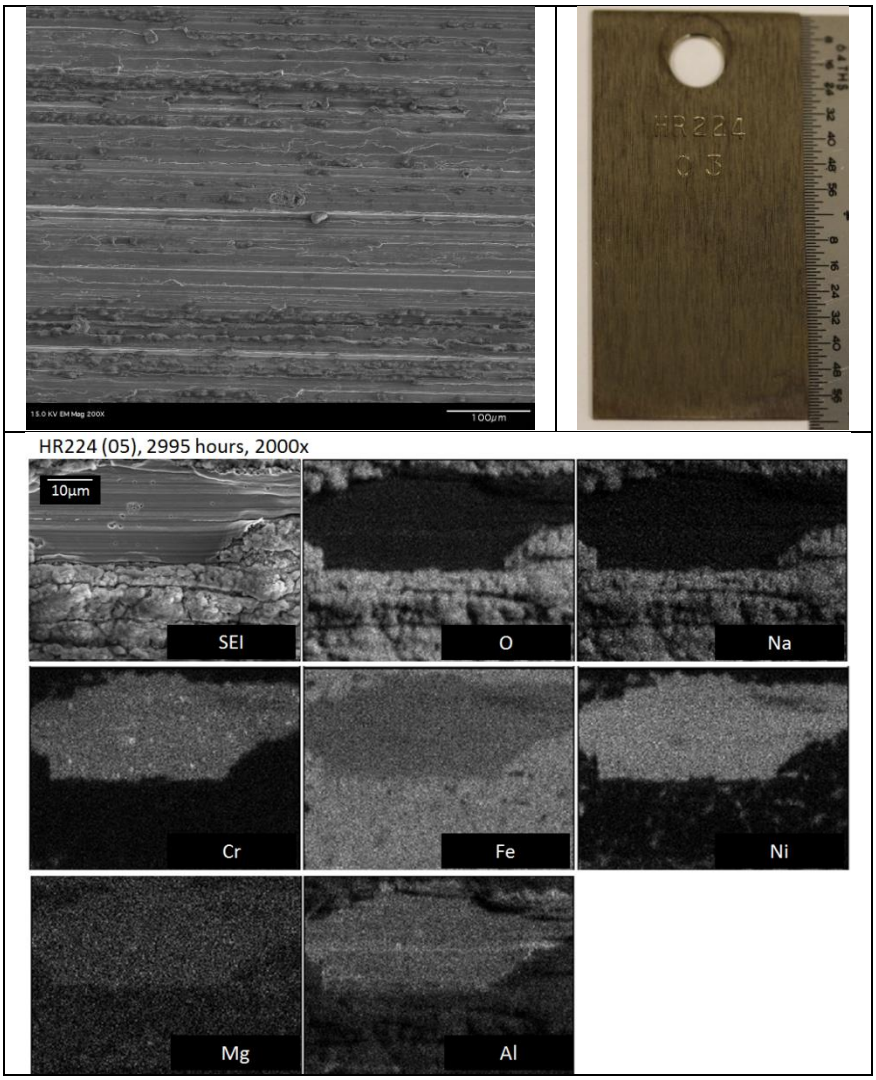

Figure 27: Plan view of HR224 after 1000 hours (top) and 2995 hours (bottom). Incomplete oxidation occurred over entirety of study, with base metal clearly visible.

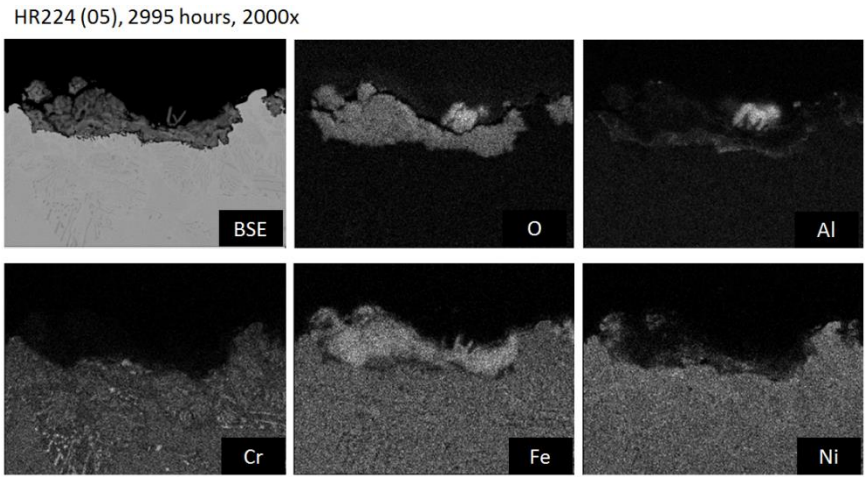

Figure 28: EDS map of HR224

iv. [Ni-Cr/Mo Alloys]

Alloys in this section were composed of primarily nickel, chromium or molybdenum, although it should be mentioned HA230 had 14%wt tungsten. Figure 29 provides a qualitative ranking with HA214 performing best, followed by In625, HA242 and HA230. Descaling was performed as listed in the analysis section, although after the chemical treatment and mechanical abrasion In625 and HA230 still exhibited noticeable discoloration and speckles due to the strong adherence of corrosion products. It was necessary to cycle chemical baths multiple times to fully descale both alloys.

Due to the amount of samples that could be fit into the test chamber only four time steps were acquired, such that a lack of statistics casts inherent uncertainty. Notion withstanding, attempts to shed light on the oxidation rate. Trends shown in Figure 29, with fits in Table 6, do appear to exhibit parabolic or parabolic-like behavior. Time dependence for In625 appeared linear, but when contrasted to previous studies [6], the resultant lack of data solidified uncertainty inherent in the measurements.

HA230 and HA242 performed similarly over the duration of this test. Morphology of corrosion products revealed dramatic differences between the alloys. HA230 formed an outer nickel oxide layer, identified as NiO from XRD data (Figure 32), with internal oxidation beneath. Within the NiO structure, WDS indicates up to five atomic percent of Na, which may be of the phase $NaNiO_2$, although this was never confirmed through XRD. The transition from NiO to internal oxidation is marked by an abrupt increase in Ni concentration (Figure 33). This transition occurred around 10microns, with the internal oxidation layer extending to nearly 20 microns. Evidence supported uniform internal oxidation, as no preferential grain boundary was observed.

Internal oxidation was not observed on alloys of similar composition to HA230, In625, and HA242. This result may be due primarily to the high concentration of tungsten in HA230. A model alloy, Ni-14wt%W, exhibited both parabolic weight gain and internal oxidation in the form of WO_3 on the oxidation front [36]. In molten nitrates any formation of WO_3 would be oxidized to WO_4^-, which is soluble and was detected in the tungsten concentration in the melt. Tungsten clustering, which has been observed elsewhere for HA230 [37], may also contribute to this oxidation behavior.

HA242 exhibited formation of NiO with confirmation by XRD (Figure 35) and WDS data (Figure 36). The sharp decrease of oxygen content is evidence that NiO acts as a diffusion barrier for oxidation of the base alloy. This alloy is akin to Hastelloy N, previously called INOR-8, which was one of the best performers in short duration tests, high temperature (677°) tests in nitrate/nitrite molten salts [38], with performance owing to the low chromium content. INOR-8 was developed for high temperature halide systems and chromium dissolution, due to its high activity, was determined to be a rate limiting step in corrosion performance [39]. As such, it would be interesting to test this alloy for compatibility with lower grade nitrate salts that have higher chloride content. HA242 compared with In625 has effective reversals of Cr and Mo.

In625 was included in the test matrix for comparison to previous tests [6], which employed thermal cycling for most of the data to simulate conditions experienced in a receiver tube. However, a primary result indicated little difference between isothermal corrosion and thermally cycled corrosion [6]. Comparing experimental results, shown in Figure 30, indicated that differences were approximately 15-25%. Differences between tests are likely a combination of data scatter, slight differences in salt chemistries, and isothermal vs. temperature cycling.

HA214 performed the best of the Ni-Cr/Mo alloys due primarily to the aluminum content in the alloy, nominally 4.5% by weight. Enrichment of Al around the formation of corrosion products (Figure 40) provide an indication of Al diffusion that acts as a diffusion barrier limiting oxidation of the base alloy. Similar behavior was observed with HR224, which will be discussed in the subsequent section. This is no surprise as high aluminum content alloys have been found to perform well in other high temperature oxidizing environments, provided aluminum content was adequate for continuous alumina formation [35].

Ni-Cr/Mo alloys generally corroded slightly faster than iron based alloys, but rates were still low. Time dependent oxidation appeared to be parabolic for many of the alloys; however, more time step data is needed to make a confident assessment here. NiO was the primary oxidation product formed on all of the nickel alloys. HA230, which is well known for its cycle fatigue strength, exhibited internal oxidation. No other alloys exhibited internal oxidation and it is currently thought that tungsten was partially responsible for this behavior. HA214 had incomplete formation of surface oxides over 3000 hours, which is likely rooted in the high Al content.

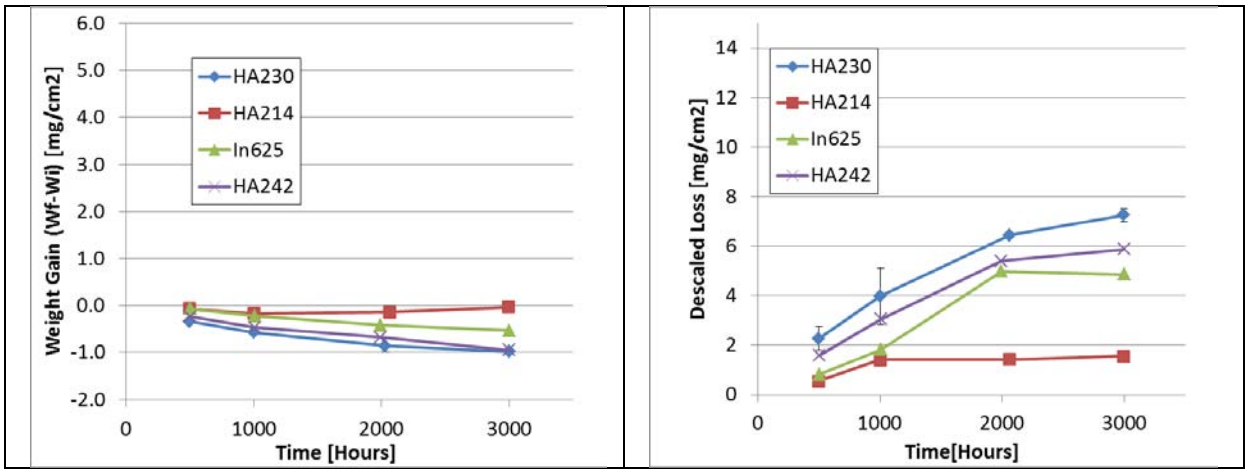

Figure 29: Weight gain and descaled weight loss of HA230, HA214, and In625

Table 6: Corrosion rate fitting parameters and extrapolated metal loss per year

Alloy	Alloy Density [g/cm^3]	Exponent Fit (n)	K [mg/ cm^2-sec^n]	Descaled Loss* [mg/cm^2]	Metal Loss* [µm/yr]
HA230[a]	8.97	0.66	1.6e-4	7.25	23.6
HA214	8.05	0.53	2.5e-4	1.56	5.7
In625	8.44	1.0	1.4e-7	4.86	16.8
HA242	9.05	0.76	2.6e-5	5.88	19.0
*Based off of 3000 hour data (Equation 3). a. Internal oxidation not accounted for in metal loss					

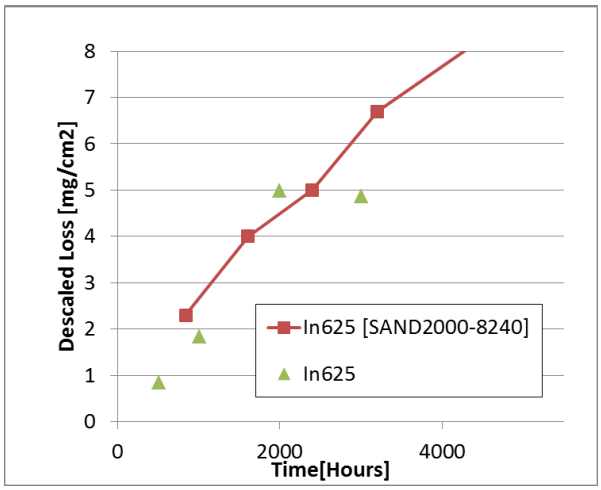

Figure 30: Comparison of weight loss data between current and past work

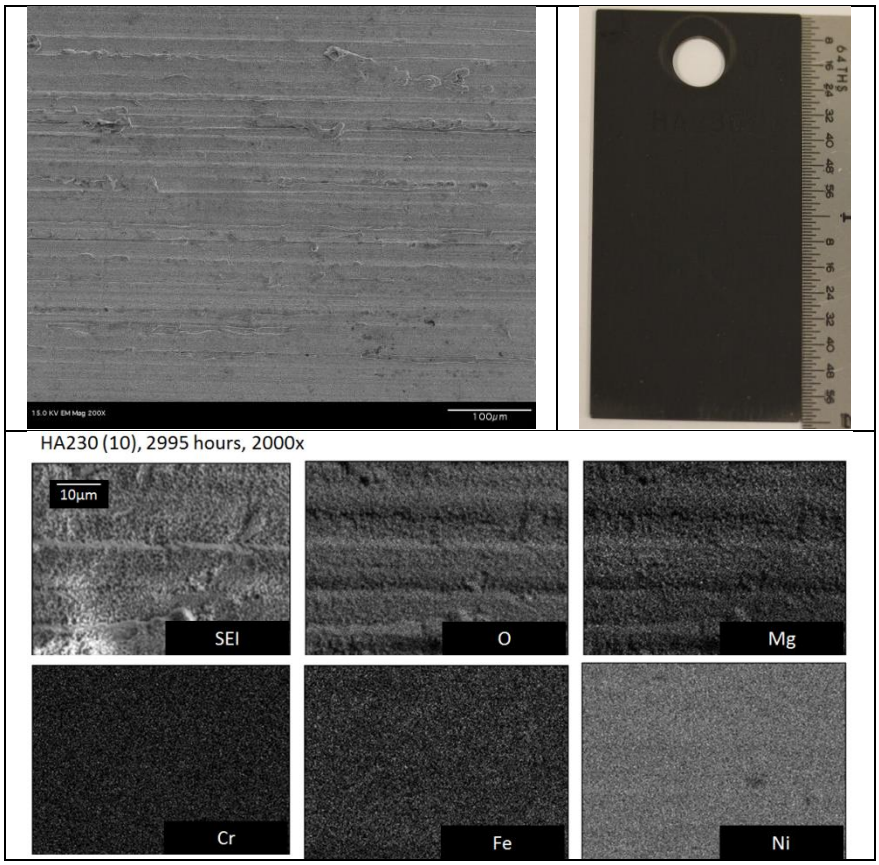

Figure 31: Plan view of HA230 after 1000 hours (top) and 2995hours (bottom). NiO was found on the surface with trace amounts of Fe and Mg present

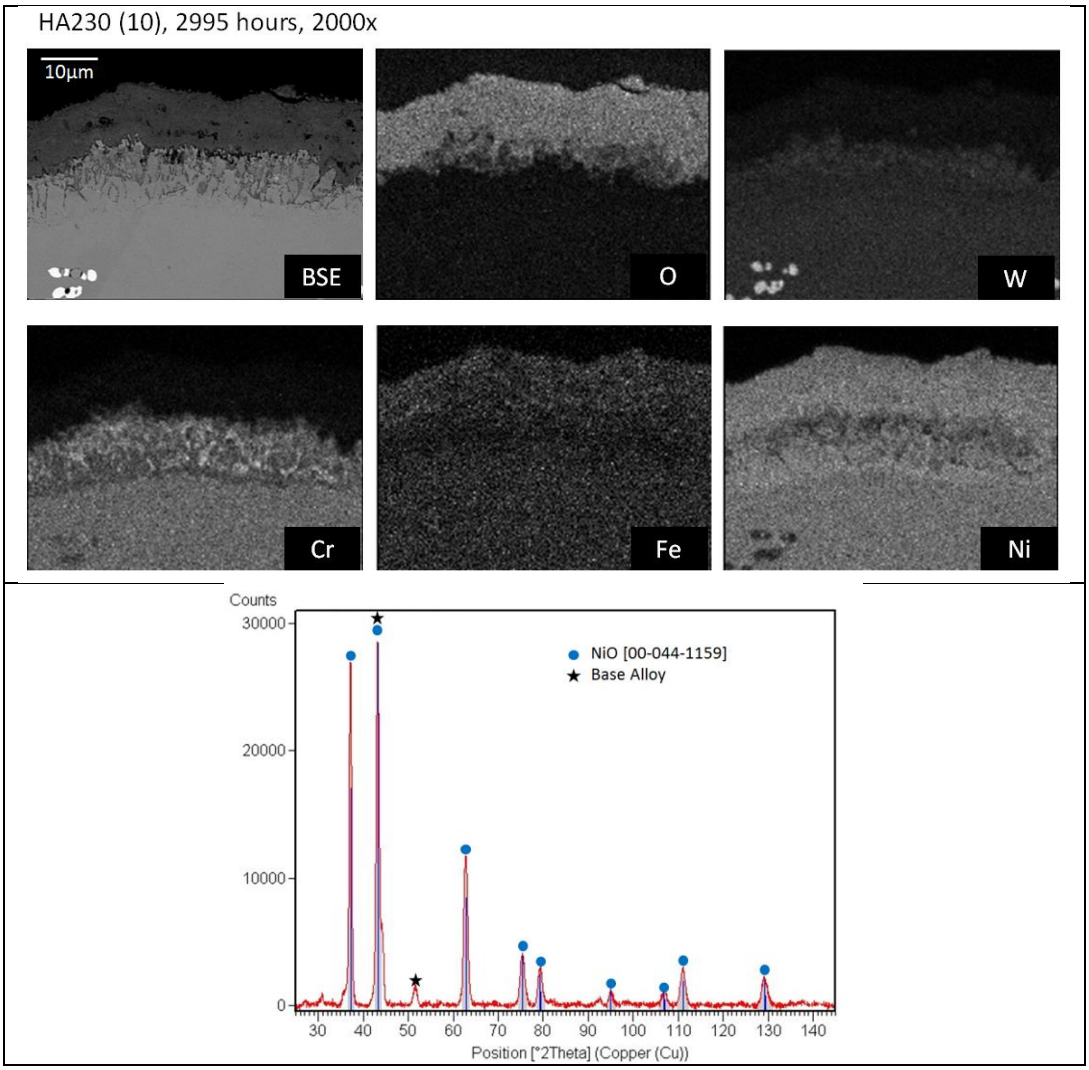

Figure 32: EDS map of HA230 with XRD data. Internal oxidation formation was observed.

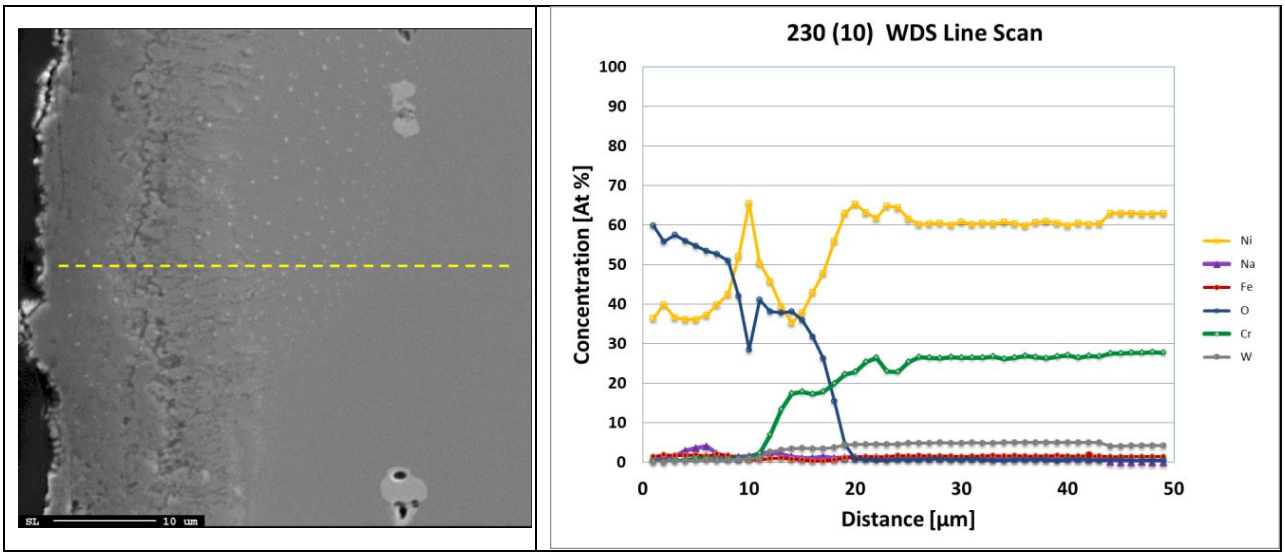

Figure 33: WDS data for HA230, showing external and internal oxidation structure and composition.

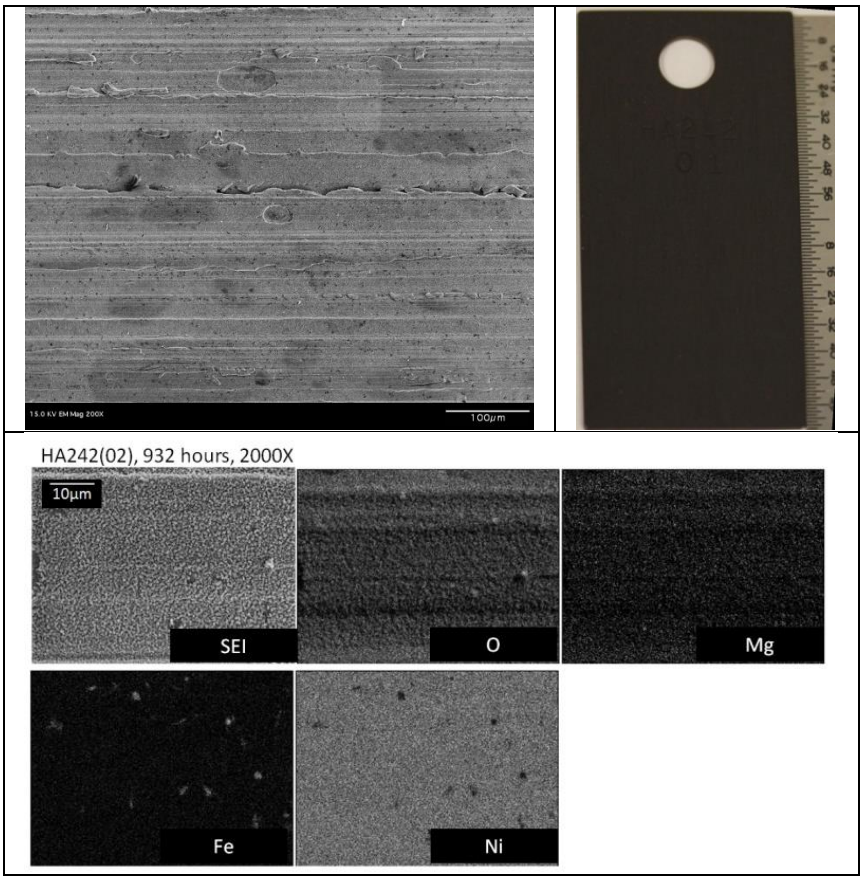

Figure 34: Plan view of HA242 after 932 hours. Dense NiO covered surface completely with trace amounts of Fe and Mg detected.

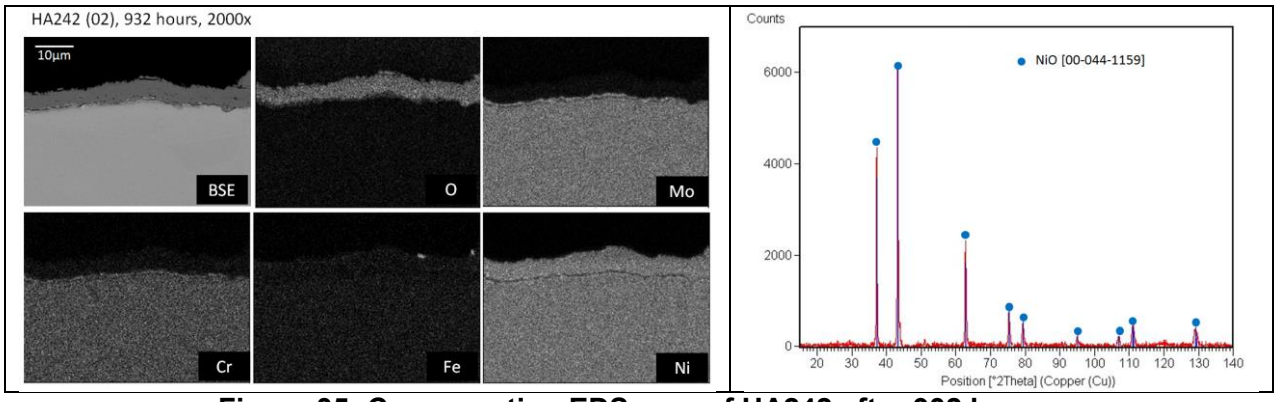

Figure 35: Cross section EDS map of HA242 after 932 hours.

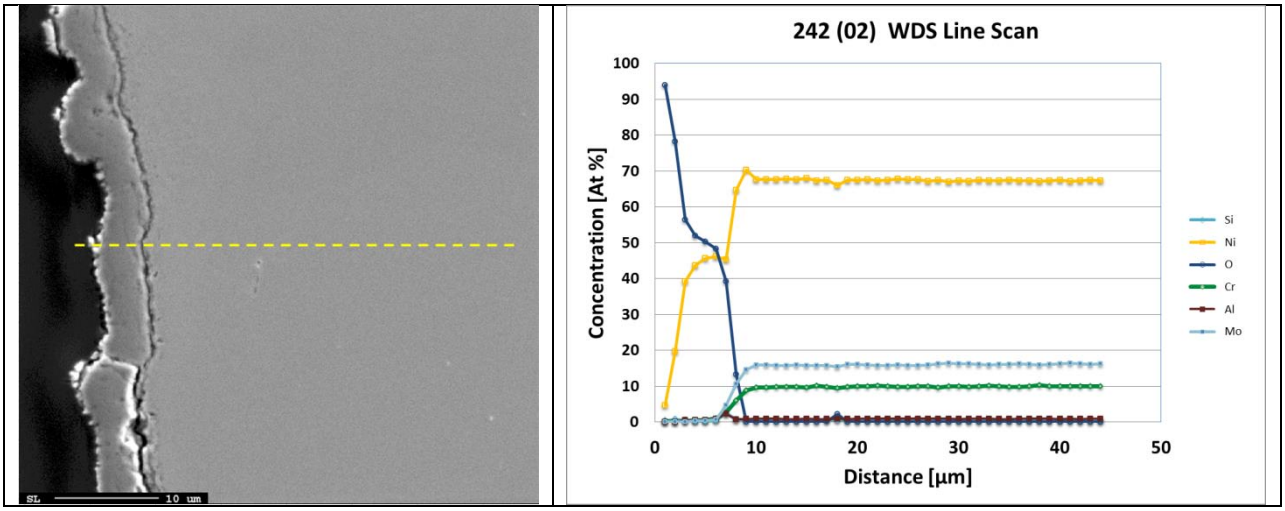

Figure 36: WDS indicates NiO as the primary phase on HA242

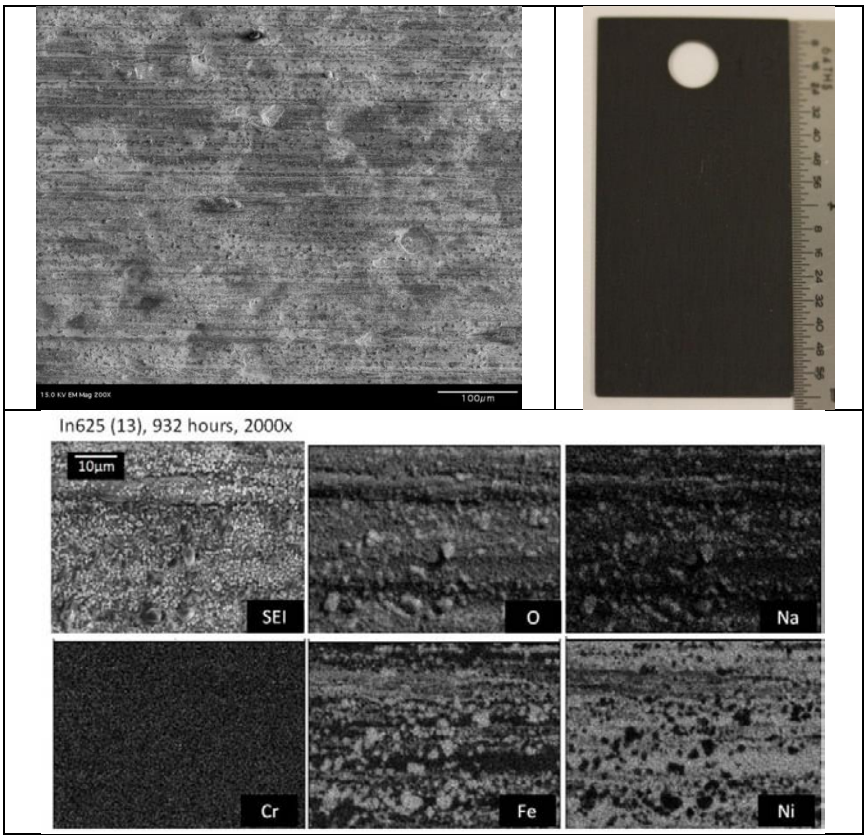

Figure 37 : Plan view of In625 after 932 hour exposure

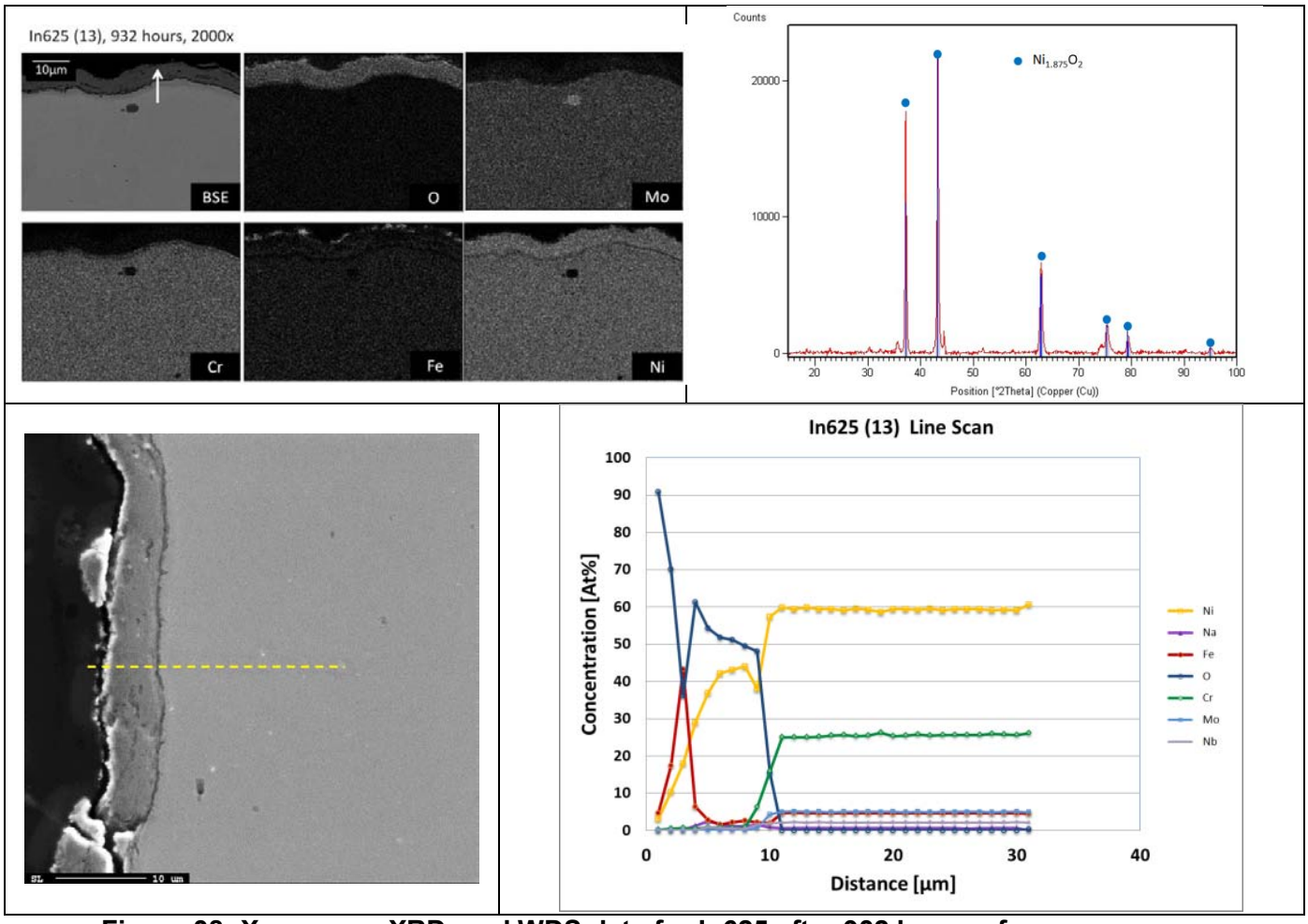

Figure 38: X-ray map, XRD, and WDS data for In625 after 932 hours of exposure.

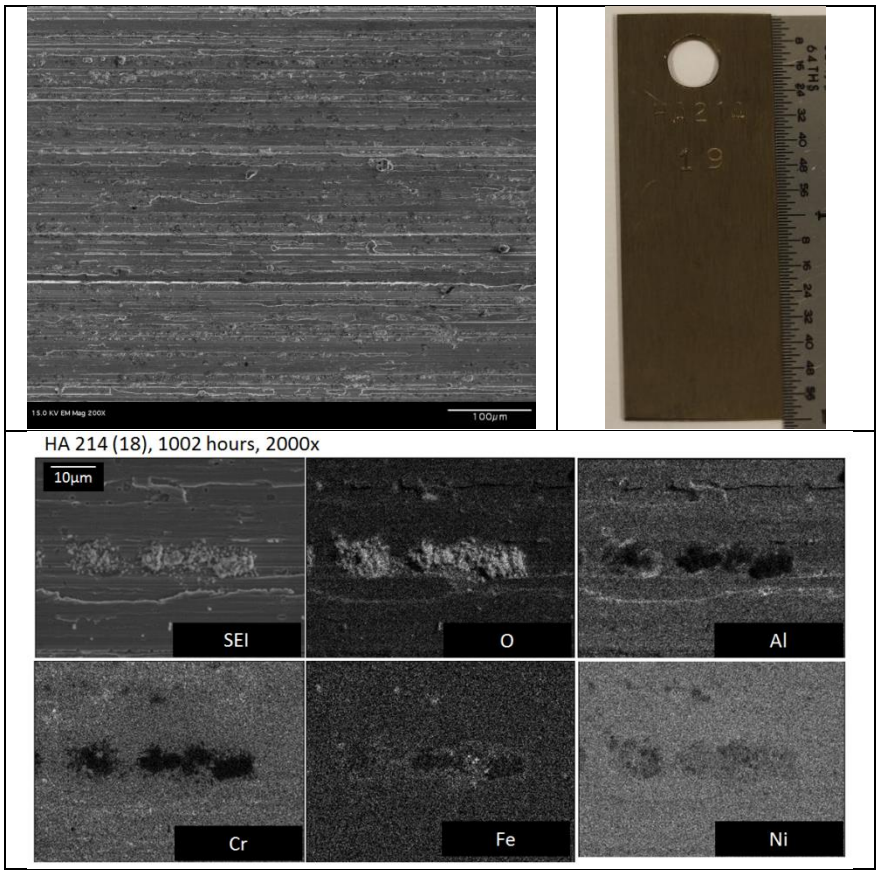

Figure 39: HA214 after 1002 hours.

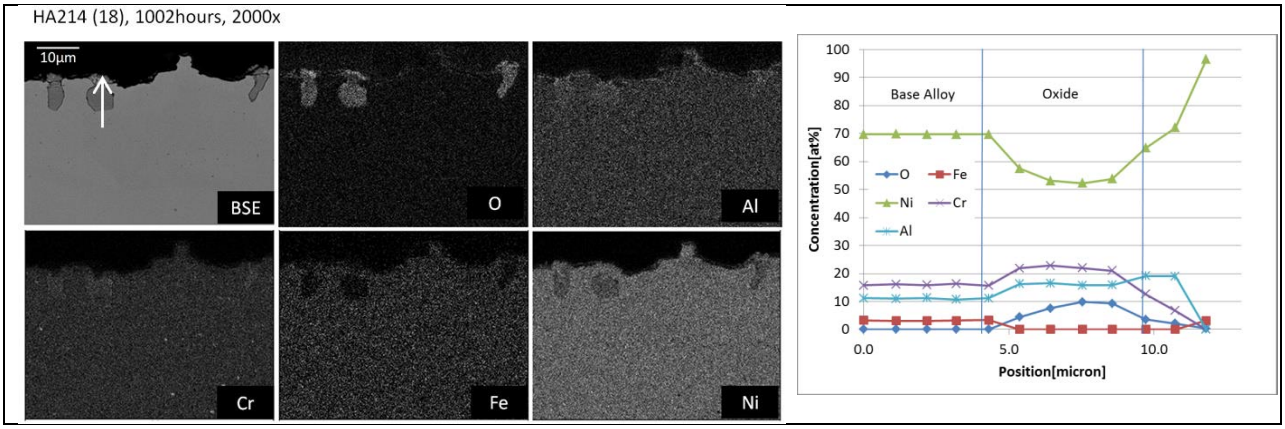

Figure 40: EDS map of HA214

4. CONCLUSIONS

Thirteen alloys were tested for corrosion performance in air sparged nitrate solar salt at 600°C. At 3000 hours a linear projection of corrosion rate (micron/year of metal loss) ranks the following alloys best to last as: HA214, HR224, S35140, 347SS, 332Mo, In625, 321SS, RA330, HR120, HA242, HA556, HA230, 253MA; as indicated in Table 7. Overall metal losses in this study were low and alloy performance was excellent. Corrosion morphology varied significantly as expected due to the spectrum of alloys tested here.

The time dependent performance of alloys was difficult to quantify primarily due to the limited time steps employed in this test. Linear vs. parabolic behavior was speculated, but further tests are needed to confidently determine the protective nature of the corrosion products formed.

Table 7: Snapshot of experimental results for all alloys with relevant parameters

Alloy	Alloy Density [g/cm^3]	Descaled Loss* [mg/cm^2]	Metal Loss* [µm/yr]	Soluble Metals [wt%]	Notes
321SS	7.94	4.59	15.9	17.6%: Cr, Mo	Spallation Observed
347SS	8.03	2.95	10.4	17.8%: Cr, Mo	
253MA	7.8	10.31	38.6	20-22%: Cr	Thick oxide layer
HA556	8.23	5.9	20.8	25.8%: Cr, Mo, W	High amount of Co
RA330	8.22	4.8	16.2	18-20%: Cr	
S35140	7.96	2.4	8.8	21-24%: Cr, Mo	
332Mo	8.13	3.4	12.2	23.4%: Cr, Mo	
HR120	8.07	4.97	18	25.2%: Cr, Mo	
HR224	8[a]	2.27	8.3	20.7%: Cr, Mo	3.8%wt - Al
HA230	8.97	7.25	23.6	37.8%: Cr, Mo, W	Internal oxidation
HA214	8.05	1.56	5.7	16%: Cr	4.5%wt - Al
In625	8.44	4.86	16.8	30.0%: Cr, Mo	
HA242	9.05	5.88	18.98	32.8%: Cr, Mo	

*Based off of 3000 hour data (Equation 3)
a. Alloy density assumed.

Fe-Cr-Ni corrosion rates were low, but lack of time step data made it difficult to confidently ascribe linear vs. parabolic kinetics to alloys tested. 347SS lost the least base metal, while 253MA lost the most. Both 321SS and 253MA appeared to exhibit time linear corrosion, with 321SS performance due surface oxide spallation. Corrosion products detected were primarily oxides involving iron and sodium, with chromium depletion present throughout the oxidation layer.

Fe-Ni-Cr alloy corrosion rates were somewhat lower than Fe-Cr-Ni, but again, lack of time step data made it difficult to confidently determine the time dependent nature of corrosion (i.e. linear vs. parabolic kinetics). S35140 and 332Mo performed the best over the duration of the test, with asymptotic increase in corrosion after 1000 hours. More data is needed to further assess the performance of these alloys, but initial results are promising. Corrosion products tended to have iron and sodium in layers exposed to salt, while inner oxides were complex mixtures of nickel, chromium and iron. Alloys exhibited nickel enrichment at the oxide/alloy interface consistently.

Ni-Fe-Cr alloy corrosion rates similar to Fe-Ni-Cr and, as previously stated, insufficient time step data made it difficult to resolve the time dependent nature of corrosion (i.e. linear vs. parabolic kinetics). HR120 had corrosion morphologies nearly identical to 332Mo, which had comparable concentrations of Ni, Fe, and Cr. HR224 performed very well, with incomplete surface oxidation even after 3000 hours. This fact was ascribed to the high concentration of Al, which would form a protective layer of Al_2O_3.

Ni-Cr/Mo alloys generally corroded slightly faster than iron based alloys, but rates were still low. Time dependent oxidation appeared to be parabolic for many of the alloys; however, more time step data is needed to make a confident assessment here. NiO was the primary oxidation product formed on all of the nickel alloys. HA230, which is well known for its cycle fatigue strength, exhibited internal oxidation. No other alloys exhibited internal oxidation and it is currently thought that tungsten was partially responsible for this behavior. HA214 had incomplete formation of surface oxides over 3000 hours, which is likely rooted in the high Al content.

Relative content of soluble transition metals (Cr/Mo/W) provided insight into the overall metal loss after 3000 hours (Figure 41). This does not provide comprehensive picture of all reactions, processes, and mechanisms, but does provide an intuition of expected performance of alloys not tested here. Future tests should be made on alloys that performed well in short term tests, with thermodynamics calculations from commercially available software packages to aide in data interpretation.

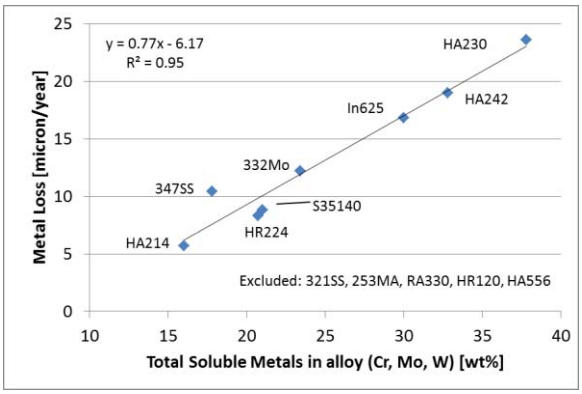

Figure 41: Effect of concentration of soluble alloying constituents on metal loss

5. REFERENCES

1. Siegel, N.P., *Thermal energy storage for solar power production.* Wiley Interdisciplinary Reviews: Energy and Environment, 2012. **1**(2): p. 119-131.
2. Pacheco, J.E., et al., *Final test and evaluation results from the Solar Two project*, 2002, SAND2002-0120, Sandia National Laboratories.
3. Burgaleta, J.I., S. Arias, and D. Ramirez, *GEMASOLAR, The First Tower Thermosolar Commerical Plant with Molten Salt Storage*, in *SolarPACES 2011,* 2011, SolarPACES: Granada, Spain.
4. Nagelberg, A.S. and R.W. Mar. *THERMOCHEMISTRY OF NITRATE SALTS*. in *Proceedings of the Symposium on High Temperature Materials Chemistry.* 1982. Denver, CO, USA: Electrochem Soc.
5. Siegel, N.P., et al., *Thermophysical Property Measurement of Nitrate Salt Heat Transfer Fluids*, in *ASME 5th International Conference on Energy Sustainability,* 2011, ASME: Washington, D.C., USA.
6. Bradshaw, R.W. and S.H. Goods, *Corrosion resistance of nickel-base alloys in molten alkali nitrates*, 2000, SAND2000-8240, Sandia National Laboratories.
7. Bradshaw, R.W. and S. Good, *Accelerated corrosion testing of a nickel-base alloy in a molten salt*, 2001, SAND2001-8758, Sandia National Laboratories.
8. Bradshaw, R.W., *THERMAL CONVECTION LOOP CORROSION TESTS OF 316SS AND IN800 IN MOLTEN NITRATE SALTS*, 1982, SAND82-8210, Sandia National Laboratories.
9. Bradshaw, R.W., *Oxidation and Chromium Depletion of Alloy 800 and 316SS by Molten NaNO3-KNO3 at Temperatures Above 600 Degrees Centigrade*, 1987, SAND86-9009, Sandia National Laboratories.
10. Bradshaw, R.W. and D.E. Meeker, *High-temperature stability of ternary nitrate molten salts for solar thermal energy systems.* Solar energy materials, 1990. **21**(1): p. 51-60.
11. Nissen, D.A. and D.E. Meeker, *NITRATE NITRITE CHEMISTRY IN NANO3-KNO3 MELTS.* INORGANIC CHEMISTRY, 1983. **22**(5): p. 716-721.
12. Gill, D.D., et al., *DESIGN, FABRICATION AND TESTING OF AN APPARATUS FOR MATERIAL COMPATIBILITY TESTING IN NITRATE SALTS AT TEMPERATURES UP TO 700°C*, in *5th International Conference on Energy Sustainability,*2011, ASME: Washington, DC, USA. p. 6.
13. Jones, D.A., *Principles and prevention of corrosion*1996, Upper Saddle River, NJ: Prentice Hall.
14. *Standard Practice for Preparing, Cleaning, and Evaluating Corrosion Test Specimens*, in *G1-03,* 2003, ASTM International.
15. Eweka, E.I. and D.H. Kerridge, *Molten sodium nitrite-sodium nitrate-potassium nitrate eutectic: the reactions and spectra of chromium(III) chloride and chromium(VI) compounds.* Thermochimica Acta, 1995. **262**(0): p. 95-100.
16. Abood, H.M.A. and D.H. Kerridge, *Thermal stability and solubility of alkaline earth nitrates and chromates in nitrate melts.* Thermochimica Acta, 1993. **215**(0): p. 183-188.
17. Kerridge, D.H. and S.A. Tariq, *Molten sodium nitrite-potassium nitrite eutectic: the reactions of some compounds of chromium.* Inorganica Chimica Acta, 1969. **3**(0): p. 667-670.

18. Freeman, E.S., *THE KINETICS OF THE THERMAL DECOMPOSITION OF SODIUM NITRATE AND OF THE REACTION BETWEEN SODIUM NITRITE AND OXYGEN.* JOURNAL OF PHYSICAL CHEMISTRY, 1956. **60**(11): p. 1487-1493.
19. Bond, B.D. and P.W.M. Jacobs, *THERMAL DECOMPOSITION OF SODIUM NITRATE.* JOURNAL OF THE CHEMICAL SOCIETY A -INORGANIC PHYSICAL THEORETICAL, 1966(9): p. 1265.
20. Kruizenga, A.M. and J.G. Cordaro, *Preliminary development of thermal stability criterion for alkali nitrates*, in *SolarPACES 2011*2011, SolarPACES: Grenada, Spain.
21. Lovering, D.G., *Molten salt technology*1982, New York: Plenum Press.
22. Nissen, D.A., *Thermophysical properties of the equimolar mixture sodium nitrate-potassium nitrate from 300 to 600.degree.C.* Journal of Chemical & Engineering Data, 1982. **27**(3): p. 269-273.
23. Afanasiev, P. and D.H. Kerridge, *Reactivity of V2O5, MoO3 and WO3 in molten KNO3, studied by mass spectrometry.* Journal of Alloys and Compounds, 2001. **322**(1-2): p. 97-102.
24. Yurkinskii, V.P., et al., *INTERACTION OF MOLYBDENUM AND TUNGSTEN WITH MOLTEN NITRATES OF ALKALI METALS.* Journal of applied chemistry of the USSR, 1984. **57**(3 pt 1): p. 476-479.
25. Goods, S.H., et al., *Corrosion of stainless and carbon steels in molten mixtures of industrial nitrates*, 1994, SAND94-8211, Sandia National Laboratories.
26. Bradshaw, R.W. and S.H. Goods, *Corrosion of alloys and metals by molten nitrates*, 2001, SAND2000-8727, Sandia National Laboratories.
27. Stott, F.H. and F.I. Wei, *High temperature oxidation of commercial austenitic stainless steels.* Materials Science and Technology, 1989. **5**(11): p. 1140-1147.
28. Pan, J., et al., *EIS study of high-temperature oxide films on a stainless steel (253MA) - influence of alloying elements.* Materials Science Forum, 1998. **289-292**(pt 2): p. 1181-1192.
29. Vangeli, P. and B. Ivarsson. *Investigation of a new methodology in high temperature oxidation application to commercial austenitic steels*. in *5th International Symposium on High Temperature Corrosion, May 22, 2000 - May 26, 2000*. 2001. Les Embiez, France: Trans Tech Publications Ltd.
30. Barin, I. and O. Knacke, *Thermochemical properties of inorganic substances*1973, Berlin; New York: Springer-Verlag.
31. Wagner, C., *Passivity and inhibition during oxidation of metals at elevated temperatures.* Corrosion Science, 1965. **5**(11): p. 751-764.
32. Abd El-Rahman, H.A., et al., *Role of oxide ion concentration on the oxidation behaviour of zirconium in molten NaNO3-KNO3 eutectic.* Thin Solid Films, 1994. **247**(1): p. 56-63.
33. Kofstad, P., *High temperature corrosion*1988, London; New York; New York, NY, USA: Elsevier Applied Science ; Sole distributor in the USA and Canada, Elsevier Science Pub. Co.
34. Matthews, W.J., K.L. More, and L.R. Walker, *Comparison of three microturbine primary surface recuperator alloys.* Journal of Engineering for Gas Turbines and Power, 2010. **132**(2).
35. Deodeshmukh, V.P., S.J. Matthews, and D.L. Klarstrom, *High-temperature oxidation performance of a new alumina-forming Ni–Fe–Cr–Al alloy in flowing air.* International Journal of Hydrogen Energy, 2011. **36**(7): p. 4580-4587.

36. Ganster, P., B. Pujilaksono, and K. Wolski. *Kinetics and mechanism of high temperature internal oxidation of Ni-14wt%W alloy at 1000C*. in *8th International Conference on Diffusion in Materials, DIMAT 2011, July 3, 2011 - July 8, 2011*. 2012. Dijon, France: Trans Tech Publications Ltd.
37. Lara-Curzio, E., et al. *Evaluation and characterization of iron- and nickel-based alloys for microturbine recuperators*. in *ASME Turbo Expo 2005 - Gas Turbie Technology: Focus for the Future, June 6, 2005 - June 9, 2005*. 2005. Reno-Tahoe, NV, United states: American Society of Mechanical Engineers.
38. Slusser, J.W., et al., *CORROSION IN MOLTEN NITRATE-NITRITE SALTS.* Journal of Metals, 1985. **37**(7): p. 24-27.
39. Williams, D.F., L.M. Toth, and K.T. Clarno, *Assessment of Candidate Molten Salt Coolants for the Advanced High-Temperature Reactor (AHTR)*, 2006, Oak Ridge National Laboratories.

Page intentionally left blank

APPENDIX:

A. Interval test

The fixed interval schedule for all samples in the test is listed in Table 8. Approximately 30 samples could be fit into each corrosion vessel, so it was necessary to divide the samples into each vessel appropriately. Table 8 also provides information on groups of samples that were in the salt simultaneously.

Table 8: Interval Test information on alloys, pull schedule, and pot configuration

Pull Schedule	Groups Removed		Group Added	Notes
500	1F		1R	
1000	2F, 3F	1R	4R,5R,6R	
2000	4F		2R	
3000	5F, 6F	2R, 4R	3R	
4000		3R, 5R, 6R	none	
Pot 1	**Forward (F)**	**Reverse (R)**	**Stainless Steels**	Descaled
	316Ti	347SS		XRD, SEM
	321SS	253MA		Descaled
	347SS	ATI20-25Nb		Descaled
	RA330	ATI332Mo		Missing 347(05), RA330(19) - > recovered at 3185
Group	**Alloys**	**Nominal Interval [hrs]**	**Actual Interval [hrs]**	Descaled
1F	316Ti (1), 321SS (01), 347SS (01), RA330 (15)	500	497	Descaled, ATI332Mo (11) is missing - > **Recovered at 3185 hrs (Run for 2688 hrs)**
2F	316Ti (2), 321SS (02), 347SS (02), RA330 (16)	1000	1001.75	XRD, SEM
3F	316Ti (4), 321SS (03), 347SS (03), RA330 (17)	1000	1001.75	Descaled
4F	316Ti (5), 321SS (04), 347SS (04), RA330 (18)	2000	2062	Descaled
5F	316Ti (6), 321SS (05), 347SS (05), RA330 (19)	3000	2995	XRD, SEM
6F	316Ti (7), 321SS (06), 347SS (06), RA330 (20)	3000	3185	Descaled
1R	347SS (08), 253MA (12), ATI20-25Nb (12), ATI332Mo (11)	500	504.45	
2R	347SS (09), 253MA (13), ATI20-25Nb (13), ATI332Mo (12)	1000	933	
3R	347SS (10), 253MA (14), ATI20-25Nb (14), ATI332Mo (13)	1000	1006	
4R	347SS (11), 253MA (15), ATI20-25Nb (15), ATI332Mo (14)	2000	2183.25	
5R	347SS (12), 253MA (16), ATI20-25Nb (16), ATI332Mo (15)	3000	2999.25	
6R	347SS (13), 253MA (17), ATI20-25Nb (17), ATI332Mo (16)	3000	2999.25	
Pot 2	**Forward (F)**	**Reverse (R)**	**Nickel Steels**	**Notes**
	Haynes 230	Haynes 556		
	Haynes 214	Hayes 230		
	HR 120	Haynes 242		
	HR 224	In 625		
Group	**Alloys**	**Nominal Interval [hrs]**	**Actual Interval [hrs]**	
1F	Haynes 230 (06), Haynes 214 (17), HR 120 (01), HR 224 (01)	500	497	Descaled
2F	Haynes 230 (07), Haynes 214 (18), HR 120 (02), HR 224 (02)	1000	1002.3	XRD/SEM
3F	Haynes 230 (08), Haynes 214 (19), HR 120 (03), HR 224 (03)	1000	1002.3	Descaled
4F	Haynes 230 (09), Haynes 214 (20), HR 120 (04), HR 224 (04)	2000	2063	Descaled
5F	Haynes 230 (10), Haynes 214 (21), HR 120 (06), HR 224 (05)	3000	2995	XRD/SEM
6F	Haynes 230 (11), Haynes 214 (22), HR 120 (05), HR 224 (06)	3000	2995	Descaled
1R	Haynes 556 (01), Haynes 230 (21), Haynes 242 (01), In625 (12)	500	505	Descaled
2R	Haynes 556 (02), Haynes 230 (22), Haynes 242 (02), In625 (13)	1000	932	Missing 556(02) - > recovered @ 3243 hrs,
3R	Haynes 556 (03), Haynes 230 (23), Haynes 242 (03), In625 (14)	1000	1006	Descaled
4R	Haynes 556 (04), Haynes 230 (24), Haynes 242 (04), In625 (15)	2000	1992.7	Descaled
5R	Haynes 556 (05), Haynes 230 (25), Haynes 242 (05), In625 (16)	3000	2998.7	XRD/SEM
6R	Haynes 556 (06), Haynes 230 (26), Haynes 242 (06), In625 (17)	3000	2998.7	Descaled

B. Additional SEM Analysis

SEM analysis and other WDS analysis, such as x-ray maps, were included in this section for completeness.

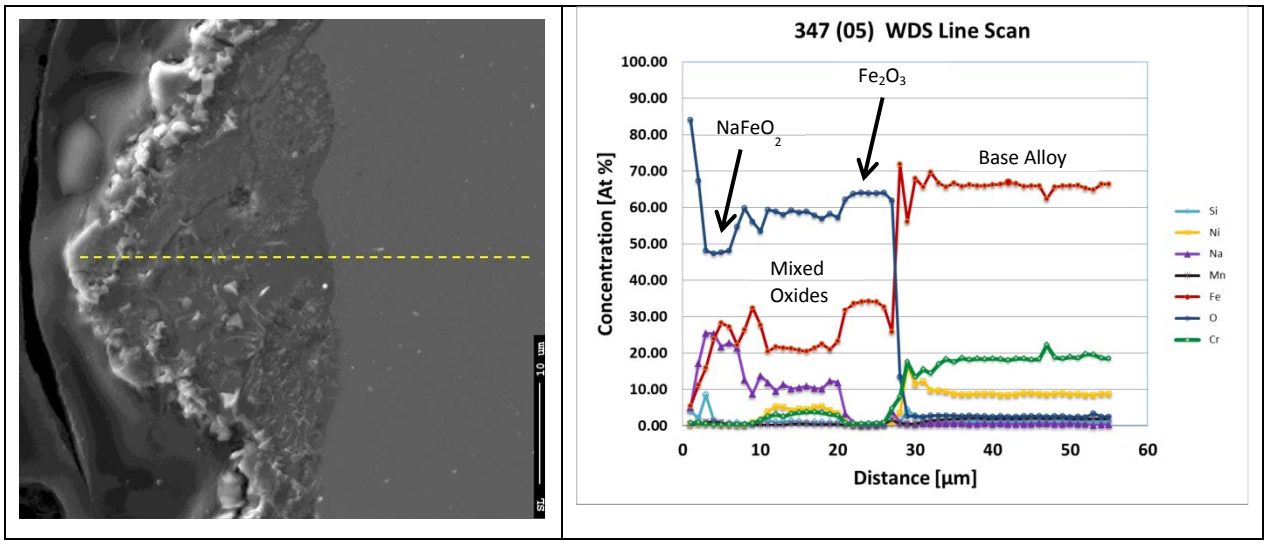

Figure 42: WDS data for 347SS after 3000 hours. Line scan provides stoichiometric data for phase composition.

C. Salt Specifications

SQM

PRODUCT DATA SHEET - INDUSTRIAL CHEMICALS

SODIUM NITRATE — Refined Grade - Thermosolar - Crystals — CAS N°7631 - 99 - 4

GENERAL DESCRIPTION	
CHEMICAL FORMULA	$NaNO_3$
APPEARANCE	White Crystals
ANTICAKING AGENT	None
INTERNAL CODE	SSR-C

CHEMICAL SPECIFICATIONS GUARANTEED				
PURITY	$NaNO_3$	%	99.5	min
TOTAL CHLORIDE [1]	as Cl	%	0.1	max
CHLORIDE	Cl	%	0.08	max
PERCHLORATE	ClO_4	%	0.035	max
MAGNESIUM	Mg	%	0.02	max
NITRITE	NO_2	%	0.02	max
SULFATE	SO_4	%	0.10	max
CARBONATE	CO_3	%	0.10	max
HYDROXIL	OH	%	0.05	max
INSOLUBLES		%	0.05	max
MOISTURE [2]		%	0.1	max

Notes
[1] The product does not contain other relevant sources of halogen compounds: Iodide, bromide, iodate, bromate or any other.
[2] Moisture measured at production site. Some absorption of moisture may occur during transportation

CHEMICAL SPECIFICATIONS TYPICAL			
MAGNESIUM	Mg	%	0.006
CALCIUM	Ca	%	0.002
NITRITE	NO_2	%	< 0.02
SULFATE	SO_4	%	0.1
IRON	Fe	ppm	< 10
LEAD	Pb	ppm	< 5
CADMIUM	Cd	ppm	< 1
CHROMIUM	Cr	ppm	< 0.5
MERCURY	Hg	ppm	< 0.5
ARSENIC	As	ppm	< 0.5
INSOLUBLES		%	0.02
MOISTURE		%	0.03

PARTICLE SIZE GUARANTEED		
Particle Size	2 mm	max

Note: Insoluble particles between 0.85 mm and 2 mm represent typically less than 0.05% of the product

SQM

PRODUCT DATA SHEET - INDUSTRIAL CHEMICALS

POTASSIUM NITRATE — Refined Grade - Thermosolar - Crystals — CAS N°7631 - 99 - 4

GENERAL DESCRIPTION	
CHEMICAL FORMULA	KNO_3
APPEARANCE	White Crystals
ANTICAKING AGENT	None
INTERNAL CODE	NPC-R

CHEMICAL SPECIFICATIONS GUARANTEED				
PURITY	KNO_3	%	99.6	min
TOTAL CHLORIDE [1]	as Cl	%	0.1	max
CHLORIDE	Cl	%	0.1	max
PERCHLORATE	ClO_4	%	0.01	max
MAGNESIUM	Mg	%	0.01	max
NITRITE	NO_2	%	0.02	max
SULFATE	SO_4	%	0.05	max
CARBONATE	CO_3	%	0.02	max
HYDROXIL	OH	%	0.01	max
INSOLUBLES		%	0.05	max
MOISTURE [2]		%	0.1	max

Notes
1 The product does not contain other relevant sources of halogen compounds: iodide, bromide, iodate, bromate or any other.
[2] Moisture measured at production site. Some absorption of moisture may occur during transportation

CHEMICAL SPECIFICATIONS TYPICAL			
MAGNESIUM	Mg	%	0.003
CALCIUM	Ca	%	0.002
NITRITE	NO_2	%	< 0.02
SULFATE	SO_4	%	< 0.01
IRON	Fe	ppm	< 10
LEAD	Pb	ppm	< 5
CADMIUM	Cd	ppm	< 1
CHROMIUM	Cr	ppm	< 0.5
MERCURY	Hg	ppm	< 0.5
ARSENIC	As	ppm	< 0.5
INSOLUBLES		%	< 0.01
MOISTURE		%	0.03

PARTICLE SIZE GUARANTEED		
Particle Size	2 mm	max

Note: Insoluble particles between 0.85 mm and 2 mm represent typically less than 0.05% of the product

DISTRIBUTION

External (electronic)

1 Joseph Stekli
US DOE Office of the Solar Energy Technology Program
Route Symbol: EE-2A
Building: L'ENF950
Washington, DC 20585

1 Bruce Kelly
Abengoa Solar
11500 West 13th Avenue
Lakewood, CO

1 David Wasyluk
Babcock & Wilcox Power Generation Group
20 S. Van Buren Avenue
Barberton, Ohio 44203

1 Greg Kolb
SolarReserve
1205 Lawrence Ct. NE
Albuquerque, NM 87112

1 Lee Flowers
Haynes International, Inc.
1020 West Park Avenue
Kokomk, IN 46904-9013

1 Matthew Bender
ATI Allegheny Ludlum
1300 Pacific Avenue
Natrona Heights, PA 15065, USA

1 Craig Tyner
eSolar
3355 W. Empire Avenue
Suite 200
Burbank, CA 91504

1 Trent Maxwell
Alstom Power
1201 Riverfront Parkway
Chattanooga TN 37402

Internal (electronic)

1	MS1127	David Gill	6123
1	MS1127	Charles Andraka	6123
1	MS1127	Subhash Shinde	6123
1	MS1127	William Kolb	6123
1	MS9153	Timothy Shepodd	8200
1	MS9402	Ryan Nishimoto	8651
1	MS9403	Alan Kruizenga	8223
1	MS9403	Adam Rowen	8223
1	MS9403	Marianne LaFord	8223
1	MS0899	Technical Library	9536


Sandia National Laboratories